Title: Transferrin receptor 1 is a reticulocyte-specific receptor for *Plasmodium vivax*

Authors: Jakub Gruszczyk[1], Usheer Kanjee[2], Li-Jin Chan[1,3], Sébastien Menant[1], Benoit Malleret[4,5], Nicholas T.Y. Lim[1], Christoph Q. Schmidt[6], Yee-Foong Mok[7], Kai-Min Lin[8], Richard D. Pearson[9,10], Gabriel Rangel[2], Brian J. Smith[11], Melissa J. Call[1,3], Michael P. Weekes[8], Michael D. W. Griffin[7], James M. Murphy[1,3], Jonathan Abraham[12], Kanlaya Sriprawat[13], Maria J. Menezes[14], Marcelo U. Ferreira[14], Bruce Russell[15], Laurent Renia[5], Manoj T. Duraisingh[2], Wai-Hong Tham[1,3,*]

Affiliations:

[1]The Walter and Eliza Hall Institute of Medical Research, Parkville, Victoria 3052, Australia.

[2]Department of Immunology and Infectious Diseases, Harvard T.H. Chan School of Public Health, Boston, Massachusetts, 02115, USA.

[3]Department of Medical Biology, The University of Melbourne, Melbourne, Victoria 3010, Australia.

[4]Department of Microbiology and Immunology, Yong Loo Lin School of Medicine, National University of Singapore, 117597 Singapore.

[5]Singapore Immunology Network, A*STAR, 138648 Singapore.

[6]Institute of Pharmacology of Natural Products and Clinical Pharmacology, Ulm University, Germany.

[7]Department of Biochemistry and Molecular Biology, Bio21 Molecular Science and Biotechnology Institute, The University of Melbourne, Melbourne, Victoria 3010, Australia.

[8]Cambridge Institute for Medical Research, Cambridge, CB2 OXY, United Kingdom.

[9]Wellcome Trust Sanger Institute, Hinxton, Cambridge, United Kingdom.

[10]Big Data Institute, Li Ka Shing Centre for Health Information and Discovery, Oxford, United Kingdom.

[11]La Trobe Institute for Molecular Science, La Trobe University, Melbourne Victoria 3086, Australia.

[12]Department of Microbiology and Immunobiology, Harvard Medical School, Boston, Massachusetts 02115, USA.

[13]Shoklo Malaria Research Unit, Mahidol-Oxford Tropical Medicine Research Unit, Faculty of Tropical Medicine, Mahidol University, Mae Sot, Thailand.

[14]Department of Parasitology, Institute of Biomedical Sciences, University of São Paulo, São Paulo, Brazil.

[15]Department of Microbiology and Immunology, University of Otago, Dunedin 9054, New Zealand.

*Corresponding author.
Email: tham@wehi.edu.au

Abstract: *Plasmodium vivax* shows a strict host tropism for reticulocytes. We identify transferrin receptor 1 (TfR1) as the receptor for *P. vivax* reticulocyte-binding protein 2b (PvRBP2b). The structure of the N-terminal domain of PvRBP2b involved in red blood cell binding was determined, elucidating the molecular basis for TfR1 recognition. TfR1 was validated as the biological target of PvRBP2b engagement by TfR1 expression knockdown analysis. TfR1 mutant cells deficient in PvRBP2b binding were refractory to invasion of *P. vivax*, but not to invasion of *P. falciparum*. Using Brazilian and Thai clinical isolates, we show that PvRBP2b monoclonal antibodies that inhibit reticulocyte binding also block *P. vivax* entry into reticulocytes. These data show that TfR1-PvRBP2b invasion pathway is critical for the recognition of reticulocytes during *P. vivax* invasion.

One Sentence Summary: Invasion of immature red blood cells by the malaria parasite, *Plasmodium vivax*, is mediated by binding to the host's transferrin receptor.

Main Text:

Of the hundreds of *Plasmodium* species, only *P. falciparum, P. vivax, P. ovale curtisi, P. ovale wallikeri, P. malariae* and *P. knowlesi* are known to infect humans. Within the human host, malaria parasites invade liver and red blood cells for replication and transmission. Blood stage infection is the major cause of all clinical symptoms in malaria, and therefore the therapeutic prevention of parasite entry into red blood cells could alleviate malarial disease. Entry into red blood cells depends on the interactions between parasite invasion ligands and their cognate red blood cell receptors of which only a handful have been identified (*1–7*). These ligand-receptor interactions initiate a cascade of molecular events that progress from initial attachment, recognition, commitment and finally penetration of the parasite into red blood cells (*8, 9*).

P. vivax is the most widely distributed human malaria parasite. This parasite has a strict preference for invasion into reticulocytes, which are very young red blood cells that are formed in the bone marrow following enucleation and released into the circulation. The reticulocyte-specific receptor involved in *P. vivax* entry has not been identified (*10*). Most studies have focused on the interaction between the *P. vivax* Duffy binding protein (PvDBP) and the red blood cell Duffy antigen receptor for chemokines (DARC) as individuals from western and central Africa lacking DARC are resistant to *P. vivax* invasion (*11*). However, recent reports have highlighted the presence of *P. vivax* in apparently DARC negative individuals suggesting that *P. vivax* may enter reticulocytes by binding to other receptors (*12–14*). Furthermore, DARC is present on both normocytes and reticulocytes and therefore this ligand-receptor interaction cannot govern selective entry into reticulocytes (*15*). To identify other parasite proteins involved in reticulocyte recognition, we focused on the *P. vivax* reticulocyte-binding protein family

(PvRBP). This protein family comprises 11 members of which several have been shown to bind reticulocytes; however, their cognate receptors have not been identified (*16–19*).

PvRBP2b binds transferrin receptor 1 to mediate recognition of reticulocytes

P. vivax preferentially invades reticulocytes expressing high levels of transferrin receptor 1 (TfR1 or CD71) (*20*). TfR1 is an essential housekeeping protein involved in cellular transport of iron into cells through binding of iron-loaded transferrin (Tf) (*21*). On circulating red blood cells, TfR1 is expressed only on reticulocytes and is progressively lost from their membranes as they mature into erythrocytes (*22*, *23*). TfR1 is a type II transmembrane glycoprotein that forms a dimer and its ectodomain consists of three subdomains: a ‘protease-like domain’ resembling the structure of zinc metalloproteinases, an ‘apical domain’ and a ‘helical domain’ responsible for dimerization (*24*). TfR1 is also a cellular receptor for New World hemorrhagic fever arenaviruses including Machupo (MACV), Junin, Guanarito and Sabiá viruses (*25*, *26*). Residues 208-212 of the TfR1 apical domain provide a critical recognition site for these viruses (*25*, *26*).

PvRBP2b is expressed in late-stage *P. vivax* parasites and recombinant PvRBP2b (residues 161 to 1,454, PvRBP2b$_{161\text{-}1454}$) binds preferentially to reticulocytes that express TfR1 (*19*, *27*). We observed that binding by recombinant PvRBP2b was abolished when reticulocytes were treated with trypsin and chymotrypsin (fig. S1, A and B). We confirmed that the combination of these proteases cleaves TfR1 and CR1 from the surface of reticulocytes, with other known malaria receptors including glycophorin A, basigin and DARC being susceptible to different sets of protease treatment (fig. S1, A and B). The profile of PvRBP2b binding is strikingly similar to the TfR1 surface expression on reticulocytes (Fig. 1A, bottom panel) and we show that the level of PvRBP2b binding is directly correlated with the levels of TfR1 on the surface of reticulocytes (fig. S1, C and D).

To determine if PvRBP2b$_{161\text{-}1454}$ binds to the population of reticulocytes that express TfR1 on their surfaces, we tested a panel of commercially available anti-TfR1 monoclonal antibodies (mAbs) for their ability to block recombinant PvRBP2b binding. Indeed, anti-TfR1 mAbs 23D10, L01.1, LT71, M-A712, MEM-189 and OKT9 inhibited PvRBP2b binding to reticulocytes by 78, 76, 33, 75, 92 and 90% respectively (Fig. 1A). M-A712 also prevents MACV pseudovirus entry (*25*, *28*). Anti-TfR1 mAbs 2B6, 13E4 and MEM-75 did not inhibit PvRBP2b binding; while their epitopes have not been mapped, we propose that these three antibodies may bind to a site on TfR1 that is not involved in the PvRBP2b interaction (Fig. 1A). To determine if this inhibition was specific to PvRBP2b$_{161\text{-}1454}$ binding, we analyzed the binding of *P. falciparum* reticulocyte binding protein-like homologue 4 (PfRh4) to its cognate receptor complement receptor 1 (CR1) (*4*). While addition of the first three complement control protein modules of CR1 (CCP 1–3) inhibited PfRh4$_{28\text{-}766}$ binding as expected (*29*), addition of anti-TfR1 mAb OKT9 did not significantly reduce PfRh4 binding (Fig. 1B). Since anti-TfR1 did not affect PfRh4 binding, these results show that TfR1 is a specific reticulocyte receptor for PvRBP2b.

To evaluate if PvRBP2b$_{161\text{-}1454}$ interacts directly with TfR1, we performed immuno-precipitation experiments using purified recombinant TfR1, Tf, and PvRBP2b$_{161\text{-}1454}$ proteins (Fig. 1C) (*30*). Using an anti-PvRBP2b mAb, we immuno-precipitated PvRBP2b in complex with TfR1 and Tf. PvRBP2b and TfR1 also formed a binary complex in the absence of Tf, demonstrating that PvRBP2b binds directly to TfR1 (Fig. 1C). The interaction between PvRBP2b and TfR1 is specific, as immuno-precipitation of PvRBP1a, PvRBP1b or PvRBP2a did not show evidence of complex formation with TfR1 (fig. S2A).

We developed a fluorescence resonance energy transfer (FRET)-based assay to monitor PvRBP2b-TfR1 complex formation where TfR1 labeled with DyLight-594 could be shown to

interact with PvRBP2b$_{161\text{-}1454}$ labeled with DyLight-488 (fig. S2B). The addition of 10-fold molar excess of unlabeled PvRBP2b$_{161\text{-}1454}$ and TfR1 competed out the labeled proteins and reduced the signal of the PvRBP2b-TfR1 FRET pair. In contrast, proteins that were unable to bind TfR1, such as PfRh4, had no effect on the FRET signal. Using this assay, we observed that anti-TfR1 mAbs 23D10, M-A712, MEM-189 and OKT9 that inhibited PvRBP2b$_{161\text{-}1454}$ reticulocyte binding also blocked PvRBP2b-TfR1 complex formation (Fig. 1D).

MACV GP1 and PvRBP2b bind to the apical domain of TfR1

The arenavirus envelope glycoprotein is the only protein on the virion surface and during maturation is processed into three subunits: the stable signal peptide (SSP), GP1 and GP2. The GP1 subunit interacts with cellular receptors and the structure of a MACV GP1-TfR1 complex shows that MACV GP1 binds to the apical domain of TfR1 (*31*, *32*). To determine if PvRBP2b interacts with a similar surface on TfR1, we examined if soluble MACV GP1 competes with PvRBP2b$_{161\text{-}1454}$ for binding to TfR1 on reticulocytes (Fig. 1E). Indeed, the addition of MACV GP1 reduced PvRBP2b$_{161\text{-}1454}$ binding to reticulocytes, albeit at a lower level of inhibition compared to the addition of anti-TfR1 mAb MEM-189. This inhibition was specific as PfRh4 binding was unaffected by addition of MACV GP1 or MEM-189, but clearly reduced with the addition of CCP 1-3 (Fig. 1E). The addition of MACV GP1 inhibited PvRBP2b-TfR1 complex formation and reduced the FRET signal to a similar extent as unlabeled PvRBP2b$_{161\text{-}1454}$ whereas addition of CCP 1-3 had negligible effect (Fig. 1F). These results indicate that MACV GP1 and PvRBP2b$_{161\text{-}1454}$ bind to an overlapping site on TfR1.

Crystal structure of the N-terminal domain of PvRBP2b

PvRBP2b is a 326 kDa protein with a putative red blood cell binding domain and a C-terminal transmembrane region (Fig. 2). We determined the crystal structure of the N-terminal

domain of PvRBP2b (residues 169 to 470, PvRBP2b$_{169\text{-}470}$), refined to 1.71 Å resolution (Fig. 2A, fig. S3, A to D, and table S1). The surface of the domain is mostly positively charged (Fig. 2B). It is predominantly an α-helical protein, comprising ten α-helices and two very short antiparallel β-sheets, each comprising of two β-strands. The crystal structure of PvRBP2b$_{169\text{-}470}$ has two disulfide bonds; one between Cys312 and Cys316 and the other between Cys240 and Cys284. This structure closely resembles the homologous domain of PvRBP2a and PfRh5, with a root mean square deviation (RMSD) of 1.7 Å and 3.7 Å over 268 and 225 aligned Cα atoms, respectively (Fig. 2C and fig. S4) (*18*, *33*, *34*). The theoretical X-ray solution scattering pattern calculated from the PvRBP2b$_{169\text{-}470}$ crystal structure coordinates shows excellent agreement with the experimental small angle X-ray scattering (SAXS) data (χ = 0.35; fig. S5, A to F, and table S2), with concordance between the crystal and solution conformations apparent from the overlay of the crystal structure and the *ab initio* calculated molecular envelope (Fig. 2D, left). We also obtained SAXS data for a longer fragment of PvRBP2b including residues 169 to 652 (fig. S6 and table S2). The reconstructed molecular envelope has a rod-like shape with a C-terminal part forming a continuous extension of the N-terminal domain (Fig. 2D, right). SAXS data for a larger fragment of PvRBP2b encompassing residues 161 to 969 indicate that the molecule adopts an elongated, boomerang-like shape, similar to that previously reported for PvRBP2a (fig. S6, A to F, fig. S7, A to D, and table S2) (*18*).

We calculated nucleotide diversity (π) and Tajima's *D* within PvRBP2b using data from the MalariaGEN *P. vivax* Genome Variation project (*35*). There was a peak in both metrics between amino acid positions 169 and 470, suggesting balancing selection within the N-terminal domain (Fig. 2E). Such signatures of balancing selection are often associated with genes or

proteins expressed on the surface of merozoites, and are likely due to interaction with the immune system.

To determine the importance of the N-terminal domain for PvRBP2b function, we generated a series of purified recombinant PvRBP2b protein fragments (Fig. 2F, tables S3 and S4). All proteins were soluble and properly folded as indicated by high α-helical content in CD spectra, in agreement with the secondary structure predictions (fig. S8, A to D). We observed that all fragments with the N-terminal domain bound reticulocytes (PvRBP2b$_{161\text{-}1454}$, PvRBP2b$_{161\text{-}969}$, PvRBP2b$_{169\text{-}813}$ and PvRBP2b$_{169\text{-}652}$) whereas their corresponding fragments without the domain did not (PvRBP2b$_{474\text{-}1454}$ and PvRBP2b$_{474\text{-}969}$) (Fig. 2G). However, the isolated N-terminal domain PvRBP2b$_{169\text{-}470}$ was unable to bind reticulocytes on its own (Fig. 2G), indicating that this fragment of PvRBP2b is necessary but not sufficient for reticulocyte binding. The shortest PvRBP2b fragment that showed binding to reticulocytes encompasses residues 169 to 652 (Fig. 2G). Our FRET-based assay showed that unlabeled recombinant fragments that bind reticulocytes inhibited PvRBP2b-TfR1 complex formation whereas recombinant fragments that did not bind reticulocytes had a negligible effect (Fig. 2H). Collectively our structural and functional analyses indicate that the N-terminal domain is necessary for binding, but requires the presence of the elongated C-terminal fragment to form a fully functional binding site.

PvRBP2b, TfR1 and Tf form a stable complex at nanomolar concentrations

Using surface plasmon resonance (SPR), we found that PvRBP2b$_{161\text{-}1454}$ interacts with TfR1 alone or with the binary complex of TfR1-Tf (Fig. 3A, top and bottom panels, respectively). We also observed similar results for the PvRBP2b$_{161\text{-}969}$ fragment with TfR1 and TfR1-Tf (Fig. 3B, top and bottom panels, respectively). These results indicate that Tf was not

required for the PvRBP2b-TfR1 complex formation, since the addition of Tf resulted in similar binding responses than for TfR1 alone. We analyzed a PvRBP2b, TfR1 and Tf ternary complex using analytical size exclusion chromatography (SEC), and used SDS-PAGE analyses to confirm co-migration of complex components. The ternary complex was detected for PvRBP2b$_{161\text{-}1454}$ and PvRBP2b$_{161\text{-}969}$ (Fig. 3, C and D, top panels respectively, and table S5). In contrast, their corresponding fragments without the N-terminal domain (PvRBP2b$_{474\text{-}1454}$ and PvRBP2b$_{474\text{-}969}$) did not form any observable ternary complexes (Fig. 3, C and D, bottom panels). The interaction between PvRBP2b and TfR1-Tf binary complex is similar in the presence of either the iron-depleted or iron-loaded form of human transferrin (fig. S2C). Furthermore, the homologous member of the same protein family, PvRBP2a, did not form a ternary complex with TfR1-Tf (fig. S2D).

Sedimentation velocity analyses of TfR1, Tf and PvRBP2b$_{161\text{-}969}$ indicated that the isolated proteins are homogenous, with weight-average sedimentation coefficients of 7.3 S, 4.9 S and 3.6 S, respectively (Fig. 3E). These values are consistent with a stable dimer of TfR1 and monomeric forms of both Tf and PvRBP2b$_{161\text{-}969}$. The empirically-fitted shape parameter value (frictional ratio) calculated for PvRBP2b$_{161\text{-}969}$ was approximately 1.8, consistent with a highly elongated structure in solution. Mixtures of TfR1-Tf and PvRBP2b$_{161\text{-}969}$-TfR1-Tf yielded single symmetrical peaks with weight-average sedimentation coefficients of 11.5 S and 11.2 S, respectively, with no peaks observed for the individual components in these samples (Fig. 3F and fig. S9). These results indicate that Tf and TfR1 form a stable binary complex in solution and that PvRBP2b$_{161\text{-}969}$ binds to this binary complex. The frictional ratio (f/f_0) for the ternary PvRBP2b$_{161\text{-}969}$-TfR1-Tf was higher than for the binary TfR1-Tf complex, resulting in a

reduction in the sedimentation coefficient on formation of the ternary complex and indicating that it has an elongated structure in solution.

Deletions in TfR1 generated via CRISPR/Cas9 abolishes PvRBP2b binding and *P. vivax* invasion

To investigate whether loss of TfR1 surface expression on red blood cells would affect PvRBP2b protein binding, we attempted to generate a knockout of the *TFRC* gene using CRISPR/Cas9 genome editing of the JK-1 erythroleukemia cell line. We obtained single cell clones that displayed reduced expression of TfR1 and validated the mutation in two independent clones (TfR1 mut1 and TfR1 mut2) (fig. S10, A to C). Both clones contained an identical -3 bp deletion that resulted in the loss of amino acid Gly217 in the TfR1 apical domain, but left the rest of the protein in-frame. TfR1 mut1 was homozygous for this deletion while TfR1 mut2 has a -3 bp as described above on one allele and a -11 bp deletion on the other allele, the latter leading to a premature stop codon. Deletion of *TFRC* in a mouse model is embryonic lethal and leads to severe disruption of erythropoiesis (*36*), suggesting that complete deletion of *TFRC* in erythroid-lineage cells, such as JK-1 may not be possible.

Differentiated polychromatic JK-1 cells (termed jkRBCs) express surface proteins (including TfR1) at levels comparable to differentiated CD34+ bone marrow-derived cultured red blood cells (cRBCs) (*37*). The jkRBCs, cRBCs and differentiated jkRBCs with a knockout within the basigin receptor (ΔBSG) show normal levels of TfR1 whereas TfR1 mutant clones displayed an intermediate level of TfR1 surface staining with a panel of anti-TfR1 mAbs (Fig. 4A and fig. S11). Levels of glycophorin A (GypA) and basigin (BSG) on these TfR1 mutant clones were similar to all control cells, showing that only TfR1 surface expression is affected on these cells (Fig. 4A). To determine if deletion of Gly217 affects PvRBP2b binding, we generated

a recombinant TfR1 protein lacking this amino acid (TfR1ΔG217). Using SEC, we show that while TfR1ΔG217 was still able to bind Tf, its binding to PvRBP2b was completely abolished (Fig. 4B). Gly217, which resides on the lateral surface of the TfR1 apical domain is close to the MACV GP1 interaction surface (fig. S10D) (*31*).

To confirm that the mutation in *TFRC* did not result in changes in expression of other red blood cells proteins, we compared the abundance of cell surface proteins between wildtype jkRBCs and the two TfR1 mutants using tandem mass tag-based quantitative surface proteomics (Fig. 4C). Out of 237 quantified surface proteins, only TfR1 and Tf were significantly modified, confirming the specificity of the *TFRC* mutations.

We next wanted to determine if PvRBP2b binding was affected in the TfR1 mutant clones. PvRBP2b$_{161\text{-}1454}$ and PvRBP2b$_{161\text{-}969}$ bound jkRBCs and cRBCs, whereas recombinant fragments PvRBP2b$_{474\text{-}1454}$ and PvRBP2b$_{474\text{-}969}$ that lacked the N-terminal domain did not (Fig. 4D). In contrast, we did not detect any PvRBP2b$_{161\text{-}1454}$ and PvRBP2b$_{161\text{-}969}$ binding to TfR1 mutant cells. This abolition of binding was specific to deletions in *TFRC* as PvRBP2b binding was unaffected on ΔBSG null cells or on cRBCs (Fig. 4D, right panel). We also compared the invasion efficiency between jkRBCs and TfR1 mutant cell lines with either Brazilian *P. vivax* isolates or *P. falciparum* 3D7 (Fig. S10E). A significant (> 10-fold) reduction in invasion efficiency was observed in the TfR1 mutant line compared to the jkRBCs line with *P. vivax*, while no significant difference was observed with *P. falciparum* (Fig. 4E). These results validate TfR1 as the cognate receptor for PvRBP2b and that TfR1 is an essential host factor for *P. vivax* invasion.

Anti-PvRBP2b antibodies block reticulocyte-binding and *P. vivax* invasion

To examine if PvRBP2b antibodies could inhibit *P. vivax* invasion, we raised mouse monoclonal antibodies to PvRBP2b$_{161\text{-}1454}$ and obtained four mAbs. 3E9, 6H1 and 10B12 bound epitopes within the N-terminal domain present in PvRBP2b$_{169\text{-}470}$ with high affinities (Fig. 5A, fig. S12, A to C, and table S6), while mAb 8G7 recognized an epitope outside the N-terminal domain within amino acids 813 to 969 (Fig. 5A). Competition ELISA experiments using mAbs directly conjugated to horseradish peroxidase (HRP) show that each mAb only competed with itself for binding to PvRBP2b, showing that 3E9, 6H1, and 10B12 bind to distinct epitopes in the N-terminal domain (Fig. 5B). Neither polyclonal nor monoclonal anti-PvRBP2b antibodies recognize recombinant PfRh4 and five other recombinant PvRBPs indicating that these antibodies are specific to PvRBP2b (fig. S12B) (*19*). Using flow cytometry, we show that addition of anti-PvRBP2b mAbs 3E9, 6H1 and 10B12 abolished the PvRBP2b$_{161\text{-}1454}$ binding to reticulocytes, whereas anti-PvRBP2b mAb 8G7 and anti-PvRBP2a mAb 3A11 had no effect (Fig. 5C).

We tested the ability of the anti-PvRBP2b antibodies to inhibit *P. vivax* invasion into human reticulocytes using a short-term *P. vivax ex vivo* assay with Brazilian and Thai clinical isolates (Fig. 5D, blue and black open dots respectively). As a control, we used a camelid anti-Fy6 antibody which is a single monovalent VHH domain (15 kDa) (*38*, *39*), that targets a surface exposed epitope on DARC and blocks its interaction with PvDBP. The addition of the 25 μg/ml camelid anti-Fy6 antibody in *ex vivo* assays using Thai isolates resulted in 85% inhibition of *P. vivax* invasion (Fig. 5D). Using four Thai isolates, the addition of inhibitory anti-PvRBP mAbs 3E9, 6H1 and 10B12 at 25 μg/ml resulted in 49%, 45% and 42% inhibition of *P. vivax* invasion, respectively. To determine if inhibition could be improved by increasing the concentration of anti-PvRBP2b mAbs to match the molarity and valency of the single VHH domain, we used 125

μg/ml of inhibitory anti-PvRBP2b mAbs. Under these conditions, we tested the invasion efficiency of two Brazilian isolates. We observed that addition of inhibitory anti-PvRBP mAbs 3E9, 6H1 and 10B12 at 125 μg/ml resulted in 68%, 45% and 57% inhibition of *P. vivax* invasion in Brazilian isolates, respectively (Fig. 5D). To enable quantitative analyses of the *ex vivo* assays, we combined our initial results of Thai and Brazilian isolates at their respective mAb concentrations. We note that increased concentration of the inhibitory anti-PvRBP2b mAbs resulted in an equivalent or small increase in inhibition of *P. vivax* invasion (Thai at 25 μg/ml vs Brazilian at 125 μg/ml). Thus, our combined sample set underestimates the level of inhibition for antibody concentrations of 125 μg/ml. As additional controls, we included the non-inhibitory anti-PvRBP2b mAb 8G7 and an IgG1 mouse isotype control which displayed only 8% and 9% inhibition of *P. vivax* invasion, respectively (Fig. 5D). These results show that addition of anti-PvRBP2b inhibitory mAbs 3E9, 6H1 and 10B12 resulted in significant reduction of *P. vivax* invasion compared to the non-inhibitory anti-PvRBP2b mAb 8G7 (Fig. 5D).

We show that the inhibitory anti-PvRBP2b mAbs target a domain that appears to be under balancing selection (Fig. 2E and Fig. 5A), which may result in differences in inhibition between clinical isolates owing to the presence of polymorphic epitopes. To circumvent inter-isolate differences, we further tested the combination of all three inhibitory mAbs, 3E9, 6H1 and 10B12 pooled together (mAb pool) and polyclonal anti-PvRBP2b antibodies. The mAb pool resulted in significant 48% reduction in *P. vivax* invasion in both Thai and Brazilian isolates compared to anti-PvRBP2b mAb 8G7 (Fig. 5D). Addition of purified total IgG of polyclonal anti-PvRBP2b R1527 antibodies resulted in 53% reduction in *P. vivax* invasion whereas the rabbit prebleed IgG only showed only 5% inhibition (Fig. 5D). A previous study using rabbit anti-PvDBP antibodies shows that *P. vivax* invasion was reduced up to 64% (*40*), a level of

inhibition comparable to what has been observed with our anti-PvRBP2b antibodies (Fig. 5D). These results show anti-PvRBP2b mAbs that block binding to reticulocytes also inhibit *P. vivax* invasion and highlight the important role of the PvRBP2b-TfR1 invasion pathway in *P. vivax* field isolates.

Our results reveal a stable interaction between PvRBP2b and TfR1, and that anti-PvRBP2b antibodies that block binding to reticulocytes also inhibit *P. vivax* invasion into human reticulocytes. *P. vivax* invasion is significantly inhibited in the presence of TfR1 mutant cells, showing that TfR1 is a critical host factor for entry into reticulocytes. We propose that the PvRBP2b-TfR1 interaction is important for the initial recognition of the target reticulocyte cells, which results in the commitment of *P. vivax* parasites for reticulocyte invasion and the subsequent engagement of PvDBP-DARC in tight junction formation leading to the successful completion of the invasion process. Identification of the molecular entities required for *P. vivax* invasion offer the possibility to target multiple invasion pathways for synergistic inhibition of *P. vivax* blood stage infection.

References and Notes:

1. A. G. Maier *et al.*, *Plasmodium falciparum* erythrocyte invasion through glycophorin C and selection for Gerbich negativity in human populations. *Nat. Med.* **9**, 87–92 (2003).

2. C. Crosnier *et al.*, Basigin is a receptor essential for erythrocyte invasion by *Plasmodium falciparum*. *Nature*. **480**, 534–537 (2011).

3. B. K. Sim, C. E. Chitnis, K. Wasniowska, T. J. Hadley, L. H. Miller, Receptor and ligand domains for invasion of erythrocytes by *Plasmodium falciparum*. *Science*. **264**, 1941–1944 (1994).

4. W.-H. Tham *et al.*, Complement receptor 1 is the host erythrocyte receptor for *Plasmodium falciparum* PfRh4 invasion ligand. *Proc. Natl. Acad. Sci. U. S. A.* **107**, 17327–17332 (2010).

5. L. H. Miller, S. J. Mason, J. A. Dvorak, M. H. McGinniss, I. K. Rothman, Erythrocyte receptors for (*Plasmodium knowlesi*) malaria: Duffy blood group determinants. *Science*. **189**, 561–563 (1975).

6. J. H. Adams *et al.*, The Duffy receptor family of *Plasmodium knowlesi* is located within the micronemes of invasive malaria merozoites. *Cell*. **63**, 141–153 (1990).

7. R. Horuk *et al.*, A receptor for the malarial parasite *Plasmodium vivax*: the erythrocyte chemokine receptor. *Science*. **261**, 1182–1184 (1993).

8. A. F. Cowman, B. S. Crabb, Invasion of red blood cells by malaria parasites. *Cell*. **124**, 755–766 (2006).

9. G. E. Weiss *et al.*, Revealing the sequence and resulting cellular morphology of receptor-ligand interactions during *Plasmodium falciparum* invasion of erythrocytes. *PLoS Pathog.* **11**, e1004670 (2015).

10. I. Mueller *et al.*, Key gaps in the knowledge of *Plasmodium vivax*, a neglected human malaria parasite. *Lancet Infect. Dis.* **9**, 555–566 (2009).

11. L. H. Miller, S. J. Mason, D. F. Clyde, M. H. McGinniss, The resistance factor to *Plasmodium vivax* in blacks. The Duffy-blood-group genotype, FyFy. *N. Engl. J. Med.* **295**, 302–304 (1976).

12. T. G. Woldearegai, P. G. Kremsner, J. F. J. Kun, B. Mordmüller, *Plasmodium vivax* malaria in Duffy-negative individuals from Ethiopia. *Trans. R. Soc. Trop. Med. Hyg.* **107**, 328–331 (2013).

13. C. Mendes *et al.*, Duffy negative antigen is no longer a barrier to *Plasmodium vivax*--molecular evidences from the African West Coast (Angola and Equatorial Guinea). *PLoS Negl. Trop. Dis.* **5**, e1192 (2011).

14. D. Ménard *et al.*, *Plasmodium vivax* clinical malaria is commonly observed in Duffy-negative Malagasy people. *Proc. Natl. Acad. Sci. U. S. A.* **107**, 5967–5971 (2010).

15. B. Malleret *et al.*, Significant biochemical, biophysical and metabolic diversity in circulating human cord blood reticulocytes. *PloS One*. **8**, e76062 (2013).

16. J. M. Carlton *et al.*, Comparative genomics of the neglected human malaria parasite *Plasmodium vivax*. *Nature*. **455**, 757–763 (2008).

17. M. R. Galinski, C. C. Medina, P. Ingravallo, J. W. Barnwell, A reticulocyte-binding protein complex of *Plasmodium vivax* merozoites. *Cell*. **69**, 1213–1226 (1992).

18. J. Gruszczyk *et al.*, Structurally conserved erythrocyte-binding domain in *Plasmodium* provides a versatile scaffold for alternate receptor engagement. *Proc. Natl. Acad. Sci. U. S. A.* **113**, E191–E200 (2016).

19. C. T. França *et al.*, *Plasmodium vivax* reticulocyte binding proteins are key targets of naturally acquired immunity in young Papua New Guinean children. *PLoS Negl. Trop. Dis.* **10**, e0005014 (2016).

20. B. Malleret *et al.*, *Plasmodium vivax*: restricted tropism and rapid remodelling of CD71 positive reticulocytes. *Blood*. **125**:1314-24 (2015).

21. Y. Cheng, O. Zak, P. Aisen, S. C. Harrison, T. Walz, Structure of the human transferrin receptor-transferrin complex. *Cell*. **116**, 565–576 (2004).

22. B. T. Pan, R. M. Johnstone, Fate of the transferrin receptor during maturation of sheep reticulocytes *in vitro*: selective externalization of the receptor. *Cell*. **33**, 967–978 (1983).

23. C. Harding, J. Heuser, P. Stahl, Receptor-mediated endocytosis of transferrin and recycling of the transferrin receptor in rat reticulocytes. *J. Cell Biol.* **97**, 329–339 (1983).

24. C. M. Lawrence *et al.*, Crystal structure of the ectodomain of human transferrin receptor. *Science*. **286**, 779–782 (1999).

25. S. R. Radoshitzky *et al.*, Transferrin receptor 1 is a cellular receptor for New World haemorrhagic fever arenaviruses. *Nature*. **446**, 92–96 (2007).

26. J. Abraham *et al.*, Host-species transferrin receptor 1 orthologs are cellular receptors for nonpathogenic new world clade B arenaviruses. *PLoS Pathog.* **5**, e1000358 (2009).

27. Z. Bozdech *et al.*, The transcriptome of *Plasmodium vivax* reveals divergence and diversity of transcriptional regulation in malaria parasites. *Proc. Natl. Acad. Sci. U. S. A.* **105**, 16290–16295 (2008).

28. G. Helguera *et al.*, An antibody recognizing the apical domain of human transferrin receptor 1 efficiently inhibits the entry of all New World hemorrhagic fever Arenaviruses. *J. Virol.* **86**, 4024–4028 (2012).

29. W.-H. Tham *et al.*, *Plasmodium falciparum* uses a key functional site in complement receptor type-1 for invasion of human erythrocytes. *Blood*. **118**, 1923–1933 (2011).

30. M. J. Bennett, J. A. Lebrón, P. J. Bjorkman, Crystal structure of the hereditary haemochromatosis protein HFE complexed with transferrin receptor. *Nature*. **403**, 46–53 (2000).

31. J. Abraham, K. D. Corbett, M. Farzan, H. Choe, S. C. Harrison, Structural basis for receptor recognition by New World hemorrhagic fever arenaviruses. *Nat. Struct. Mol. Biol.* **17**, 438–444 (2010).

32. S. R. Radoshitzky *et al.*, Receptor determinants of zoonotic transmission of New World hemorrhagic fever arenaviruses. *Proc. Natl. Acad. Sci. U. S. A.* **105**, 2664–2669 (2008).

33. K. E. Wright *et al.*, Structure of malaria invasion protein RH5 with erythrocyte basigin and blocking antibodies. *Nature*. **515**, 427–430 (2014).

34. L. Chen *et al.*, Crystal structure of PfRh5, an essential *P. falciparum* ligand for invasion of human erythrocytes. *eLife*. **3** (2014), doi:10.7554/eLife.04187.

35. R. D. Pearson *et al.*, Genomic analysis of local variation and recent evolution in *Plasmodium vivax*. *Nat. Genet.* **48**, 959–964 (2016).

36. J. E. Levy, O. Jin, Y. Fujiwara, F. Kuo, N. C. Andrews, Transferrin receptor is necessary for development of erythrocytes and the nervous system. *Nat. Genet.* **21**, 396–399 (1999).

37. A. K. Bei, C. Brugnara, M. T. Duraisingh, *In vitro* genetic analysis of an erythrocyte determinant of malaria infection. *J. Infect. Dis.* **202**, 1722–1727 (2010).

38. D. Smolarek *et al.*, A recombinant dromedary antibody fragment (VHH or nanobody) directed against human Duffy antigen receptor for chemokines. *Cell. Mol. Life Sci. CMLS.* **67**, 3371–3387 (2010).

39. J. S. Cho *et al.*, Unambiguous determination of *Plasmodium vivax* reticulocyte invasion by flow cytometry. *Int. J. Parasitol.* **46**, 31–39 (2016).

40. B. T. Grimberg *et al.*, *Plasmodium vivax* invasion of human erythrocytes inhibited by antibodies directed against the Duffy binding protein. *PLoS Med.* **4**, e337 (2007).

41. F. van den Ent, J. Löwe, RF cloning: a restriction-free method for inserting target genes into plasmids. *J. Biochem. Biophys. Methods*. **67**, 67–74 (2006).

42. J. Hietanen *et al.*, Gene models, expression repertoire, and immune response of *Plasmodium vivax* reticulocyte binding proteins. *Infect. Immun.* **84**, 677–685 (2016).

43. J. A. Lebrón *et al.*, Crystal structure of the hemochromatosis protein HFE and characterization of its interaction with transferrin receptor. *Cell*. **93**, 111–123 (1998).

44. A. R. Aricescu, W. Lu, E. Y. Jones, A time- and cost-efficient system for high-level protein production in mammalian cells. *Acta Crystallogr. D Biol. Crystallogr.* **62**, 1243–1250 (2006).

45. N. G. James, A. B. Mason, Protocol to determine accurate absorption coefficients for iron-containing transferrins. *Anal. Biochem.* **378**, 202–207 (2008).

46. U. Kanjee *et al.*, CRISPR/Cas9 knockouts reveal genetic interaction between strain-transcendent erythrocyte determinants of *Plasmodium falciparum* invasion. *Proc. Natl. Acad. Sci. U. S. A.* **114**, E9356–E9365 (2017).

47. N. E. Sanjana, O. Shalem, F. Zhang, Improved vectors and genome-wide libraries for CRISPR screening. *Nat. Methods*. **11**, 783–784 (2014).

48. J. G. Doench *et al.*, Optimized sgRNA design to maximize activity and minimize off-target effects of CRISPR-Cas9. *Nat. Biotechnol.* **34**, 184–191 (2016).

49. J. Moffat *et al.*, A lentiviral RNAi library for human and mouse genes applied to an arrayed viral high-content screen. *Cell*. **124**, 1283–1298 (2006).

50. E. K. Brinkman, T. Chen, M. Amendola, B. van Steensel, Easy quantitative assessment of genome editing by sequence trace decomposition. *Nucleic Acids Res.* **42**, e168 (2014).

51. E. S. Egan *et al.*, Malaria. A forward genetic screen identifies erythrocyte CD55 as essential for *Plasmodium falciparum* invasion. *Science*. **348**, 711–714 (2015).

52. M. P. Weekes *et al.*, Quantitative temporal viromics: an approach to investigate host-pathogen interaction. *Cell*. **157**, 1460–1472 (2014).

53. G. C. McAlister *et al.*, MultiNotch MS3 enables accurate, sensitive, and multiplexed detection of differential expression across cancer cell line proteomes. *Anal. Chem.* **86**, 7150–7158 (2014).

54. J. Cox, M. Mann, MaxQuant enables high peptide identification rates, individualized p.p.b.-range mass accuracies and proteome-wide protein quantification. *Nat. Biotechnol.* **26**, 1367–1372 (2008).

55. T. G. Battye, L. Kontogiannis, O. Johnson, H. R. Powell, A. G. Leslie, iMOSFLM: a new graphical interface for diffraction-image processing with MOSFLM. *Acta Crystallogr Biol Crystallogr*. **67**, 271–81 (2011).

56. M. D. Winn *et al.*, Overview of the CCP4 suite and current developments. *Acta Crystallogr Biol Crystallogr*. **67**, 235–42 (2011).

57. K. A. Kantardjieff, B. Rupp, Matthews coefficient probabilities: Improved estimates for unit cell contents of proteins, DNA, and protein-nucleic acid complex crystals. *Protein Sci*. **12**, 1865–71 (2003).

58. A. J. McCoy *et al.*, Phaser crystallographic software. *J Appl Crystallogr*. **40**, 658–674 (2007).

59. P. D. Adams *et al.*, PHENIX: a comprehensive Python-based system for macromolecular structure solution. *Acta Crystallogr Biol Crystallogr*. **66**, 213–21 (2010).

60. P. Emsley, B. Lohkamp, W. G. Scott, K. Cowtan, Features and development of Coot. *Acta Crystallogr Biol Crystallogr*. **66**, 486–501 (2010).

61. J. Painter, E. A. Merritt, TLSMD web server for the generation of multi-group TLS models. *J Appl Crystallogr*. **39**, 109–111 (2006).

62. J. M. Murphy *et al.*, The pseudokinase MLKL mediates necroptosis via a molecular switch mechanism. *Immunity*. **39**, 443–453 (2013).

63. P. V. Konarev, V. V. Volkov, A. V. Sokolova, M. H. J. Koch, D. I. Svergun, PRIMUS: a Windows PC-based system for small-angle scattering data analysis. *J Appl Crystallogr*. **36**, 1277–1282 (2003).

64. L. Liu, L. Boldon, M. Urquhart, X. Wang, Small and Wide Angle X-ray Scattering studies of biological macromolecules in solution. *J. Vis. Exp. JoVE* (2013), doi:10.3791/4160.

65. D. Svergun, C. Barberato, M. H. J. Koch, *CRYSOL* – a program to evaluate X-ray solution scattering of biological macromolecules from atomic coordinates. *J. Appl. Crystallogr.* **28**, 768–773 (1995).

66. D. Franke, D. I. Svergun, DAMMIF, a program for rapid *ab-initio* shape determination in small-angle scattering. *J Appl Crystallogr*. **42**, 342–346 (2009).

67. V. V. Volkov, D. I. Svergun, Uniqueness of *ab initio* shape determination in small-angle scattering. *J. Appl. Crystallogr.* **36**, 860–864 (2003).

68. P. Chacón, W. Wriggers, Multi-resolution contour-based fitting of macromolecular structures. *J. Mol. Biol.* **317**, 375–384 (2002).

69. W. L. DeLano, PyMOL molecular viewer: Updates and refinements. *Abstr. Pap. Am. Chem. Soc.* **238** (2009).

70. P. Schuck, P. Rossmanith, Determination of the sedimentation coefficient distribution by least-squares boundary modeling. *Biopolymers*. **54**, 328–41 (2000).

71. S. E. Harding, A. J. Rowe, J. C. Horton, Eds., *Analytical ultracentrifugation in biochemistry and polymer science /* (Royal Society of Chemistry, Cambridge [England] :, c1992.).

72. L. Whitmore, B. A. Wallace, Protein secondary structure analyses from circular dichroism spectroscopy: methods and reference databases. *Biopolymers*. **89**, 392–400 (2008).

73. L. Whitmore, B. A. Wallace, DICHROWEB, an online server for protein secondary structure analyses from circular dichroism spectroscopic data. *Nucleic Acids Res.* **32**, W668-673 (2004).

74. N. Sreerama, R. W. Woody, Estimation of protein secondary structure from circular dichroism spectra: comparison of CONTIN, SELCON, and CDSSTR methods with an expanded reference set. *Anal. Biochem.* **287**, 252–260 (2000).

75. A. Abdul-Gader, A. J. Miles, B. A. Wallace, A reference dataset for the analyses of membrane protein secondary structures and transmembrane residues using circular dichroism spectroscopy. *Bioinforma. Oxf. Engl.* **27**, 1630–1636 (2011).

76. A. M. Waterhouse, J. B. Procter, D. M. A. Martin, M. Clamp, G. J. Barton, Jalview Version 2--a multiple sequence alignment editor and analysis workbench. *Bioinforma. Oxf. Engl.* **25**, 1189–1191 (2009).

77. B. Russell *et al.*, A reliable *ex vivo* invasion assay of human reticulocytes by *Plasmodium vivax*. *Blood*. **118**, e74-81 (2011).

78. C. Lim *et al.*, Expansion of host cellular niche can drive adaptation of a zoonotic malaria parasite to humans. *Nat. Commun.* **4**, 1638 (2013).

79. C. Lim *et al.*, Improved light microscopy counting method for accurately counting *Plasmodium* parasitemia and reticulocytemia. *Am. J. Hematol.* **91**, 852–855 (2016).

80. U. W. Arndt, R. A. Crowther, J. F. Mallett, A computer-linked cathode-ray tube microdensitometer for x-ray crystallography. *J. Sci. Instrum.* **1**, 510–516 (1968).

81. M. S. Weiss, R. Hilgenfeld, On the use of the merging *R* factor as a quality indicator for X-ray data. *J. Appl. Crystallogr.* **30**, 203–205 (1997).

82. P. A. Karplus, K. Diederichs, Linking crystallographic model and data quality. *Science*. **336**, 1030–1033 (2012).

83. M. P. Weekes *et al.*, Proteomic plasma membrane profiling reveals an essential role for gp96 in the cell surface expression of LDLR family members, including the LDL receptor and LRP6. *J. Proteome Res.* **11**, 1475–1484 (2012).

Acknowledgments: We thank Janet Newman from CSIRO Collaborative Crystallization Centre for assistance with setting up the crystallization screens, the Walter and Eliza Hall Institute's Monoclonal Antibody Facility for production of antibodies, James Williamson for assistance with mass spectrometry and MX and SAXS beamline staff at the Australian Synchrotron for their assistance during data collection. We thank Prof. François Nosten, the staff and patients attending the Mae Sot Malaria Clinic, in Thailand and clinics associated with the Shoklo Malaria Research Unit (SMRU), Tak Province, Thailand. We thank also Professors Yves Colin and Olivier S. Bertrand (INSERM/University Paris 7) for the generous gift of the anti-DARC antibodies. WHT is a Howard Hughes Medical Institute-Wellcome Trust International Research Scholar. This work was supported in part by the Australian Research Council Future Fellowships to WHT and MDWG, a Speedy Innovation Grant to WHT and a National Health and Medical Research Council fellowship (1105754) to JMM. UK was supported by a Canadian Institutes of Health Research Postdoctoral Fellowship. R.D.P. is funded by Wellcome Trust 090770. Genotypes were derived from sequence data generated at the Wellcome Trust Sanger Institute

(Wellcome Trust 206194, 098051). MPW was supported by a Wellcome Trust Senior Clinical Research Fellowship (108070/Z/15/Z). This study received funding from Singapore National Medical Research Council (NMRC/CBRG/0047/2013) and the Agency for Science, Technology and Research (A*STAR, Singapore). SMRU is sponsored by The Wellcome Trust of Great Britain, as part of the Oxford Tropical Medicine Research Programme of Wellcome Trust-Mahidol University. The authors acknowledge the Victorian State Government Operational Infrastructure Support and Australian Government NHMRC IRIISS. All data and code to understand and assess the conclusions of this research are available in the main text, supplementary materials and via the following repositories: The atomic coordinates and structure factors for PvRBP2b have been deposited in Protein Data Bank with accession number 5W53.

Supplementary Materials:

Materials and Methods

Figs. S1 to S12

Tables S1 to S6

References (41-83)

Other Supplementary Material for this manuscript includes the following:

Dataset S1

Fig. 1: PvRBP2b binds TfR1 on the reticulocyte surface. (A). PvRBP2b$_{161-1454}$ binding in the presence of anti-TfR1 mAbs analysed by flow cytometry. Left: Dot plots of PvRBP2b$_{161-1454}$ binding (y-axis) to reticulocytes stained with thiazole orange (TO, x-axis). Right: normalized binding results where PvRBP2b$_{161-1454}$ binding in the absence of mAbs was arbitrarily assigned to be 100%. **(B)** PvRBP2b$_{161-1454}$ and PfRh4$_{28-766}$ binding were evaluated by flow cytometry with the addition of anti-TfR1 mAb OKT9 or CCP 1-3. PvRBP2b$_{161-1454}$ and PfRh4 binding in buffer were arbitrarily assigned to be 100%. **(C)** Eluates of individual or mixtures of proteins immuno-precipitated with anti-PvRBP2b mAb analyzed by SDS-PAGE. + or – indicates protein present or absent. Molecular weight marker (M). **(D)** Anti-TfR1 mAbs inhibit PvRBP2b-TfR1 complex formation in the FRET-based assay. The FRET signal was relative to "no mAb" control. **(E)** Binding of PvRBP2b$_{161-1454}$ and PfRh4$_{28-766}$ in the presence of anti-TfR1 mAb MEM-189, CCP 1-3 and MACV GP1. Left: dot plots showing PvRBP2b$_{161-1454}$ (top) and PfRh4$_{28-766}$ binding (bottom). Right: normalized binding results where PvRBP2b$_{161-1454}$ and PfRh4$_{28-766}$ binding in the presence of buffer was arbitrarily assigned to be 100%. **(F)** MACV GP1 inhibits PvRBP2b$_{161-1454}$-TfR1 complex formation monitored by FRET assay. For (A), (B), (D), (E) and (F), Mean ± S.E.M., $n \geq 3$, open dots represent biological replicates. Mann-Whitley test was used for (A) and (D) where MEM-75 was considered non-inhibitory and t-tests was used for (B), (E) and (F), * $P \leq 0.05$, ** $P \leq 0.001$.

Fig. 2: Crystal structure of the N-terminal domain of PvRBP2b and its functional requirement. (A) Structure of the N-terminal domain of PvRBP2b from amino acid 169 to 470 shown in two orthogonal views. **(B)** Electrostatic surface potential on the PvRBP2b structure. **(C)** Superimposition of the PvRBP2b structure (green) with PvRBP2a (purple) and PfRh5 (orange). The PDB ID codes for PfRh5 and PvRBP2a are 4WAT and 4Z8N, respectively. **(D)**

Crystal structure of the N-terminal domain superimposed with SAXS *ab initio* bead model of PvRBP2b$_{169\text{-}470}$ (left) and PvRBP2b$_{169\text{-}652}$ (right). **(E)** Sliding window analysis showing nucleotide diversity (π) values and Tajima's *D* statistic in PvRBP2b. The grey box refers to a highly polymorphic region at amino acid positions 169 to 470 that appears to be under balancing selection. **(F)** Schematic representation of full-length PvRBP2b and recombinant protein fragments (left). Signal peptide (SP), transmembrane domain (TM) and N-terminal domain (yellow) are indicated. **(G)** PvRBP2b binding results by flow cytometry where PvRBP2b$_{161\text{-}1454}$ binding was arbitrarily assigned to be 100%. **(H)** Unlabeled recombinant PvRBP2b fragments or PfRh4 were mixed at 10-fold molar excess relative to the labeled PvRBP2b$_{161\text{-}1454}$-TfR1 FRET pair. The FRET intensity was relative to buffer control. For (G to H), Mean ± S.E.M, $n = 4$, open dots represent biological replicates. The Mann-Whitley test was used to calculate the P value using the binding of 2b$_{474\text{-}1454}$ that was considered no binding, * $P \leq 0.05$, ** $P \leq 0.001$.

Fig. 3: PvRBP2b binds to TfR1-Tf to form a stable ternary complex. PvRBP2b$_{161\text{-}1454}$ **(A)** and PvRBP2b$_{161\text{-}969}$ **(B)** were coupled covalently to a biosensor chip to probe binding of TfR1 (concentration range assayed: 2 μM to 7.5 nM, top panels) and TfR1-Tf complexes (concentration range of TfR1-Tf complexes assayed: 2 μM:4 μM to 1.8 nM:3.9 nM (A) and 2 μM:4 μM to 7.5 nM:15 nM (B), bottom panels). **(C)** and **(D)** Complex formation between PvRBP2b, TfR1 and Tf analyzed by analytical size exclusion chromatography (SEC). PvRBP2b-TfR1-Tf ternary complex can be observed for PvRBP2b$_{161\text{-}1454}$ **(C, top panel)** and PvRBP2b$_{161\text{-}969}$ **(D, top panel)**. Two corresponding truncations of the N-terminal domain, PvRBP2b$_{474\text{-}1454}$ **(C, bottom panel)** and PvRBP2b$_{474\text{-}969}$ **(D, bottom panel)** do not interact with the TfR1-Tf binary complex. The exclusion volume (V_0) of the columns and the elution volumes of selected marker proteins are indicated with black arrowheads. **Lower part:** Coomassie-Blue stained

SDS-PAGE gels of the fractions obtained from SEC. **(E-F)** Continuous sedimentation coefficient distributions derived from fitting sedimentation velocity data to a *c*(*s*) sedimentation model. **(E)** *c*(*s*) distributions for TfR1 (black line), Tf (magenta line) and PvRBP2b$_{161\text{-}969}$ (blue line). **(F)** *c*(*s*) distributions for the TfR1-Tf complex (red line), and PvRBP2b$_{161\text{-}969}$-TfR1-Tf complex (green line).

Fig. 4: Deletions in *TFRC* reduce TfR1 surface expression, abolish PvRBP2b binding and inhibit *P. vivax* invasion. (A) Expression of TfR1, BSG and GYPA on the surface of jkRBCs, TfR1 mutants, ΔBSG null and cultured erythrocytes (cRBCs) as measured by flow cytometry. The right most panels show cytospin analysis of cells stained with May-Grünwald Giemsa staining technique. **(B)** TfR1ΔG217 mutation in TfR1 abrogates PvRBP2b binding as observed using analytical SEC. **(C)** Quantitative surface proteomics demonstrate specific reduction in TfR1 protein levels in TfR1 mutants compared to wildtype jkRBCs. Levels of Tf, the binding partner for TfR1, are similarly reduced. Significance A was used to estimate p-values, and a minimum of 2 peptides were required for protein quantitation. **(D)** Binding of recombinant PvRBP2b fragments to jkRBCs, TfR1mutants, ΔBSG and cRBCs cells are shown in blue. Negative controls of unstained cells and isotype control stained cells are shown in the white and orange lines respectively. Compilation of results from PvRBP2b fragment binding to jkRBCs, TfR1 mutants, ΔBSG and cRBCs (right panel). Mean ± S.E.M, n = 3. **(E)** Comparison of invasion efficiency between jkRBCs and TfR1 mutant cell lines with either *P. vivax* or *P. falciparum*. The data shown are averages and the standard error of the mean from between four to five biological replicates shown as open dots. P value was calculated using a paired, two-tailed T test, **** $P \leq 0.0001$ and ns is non-significant.

Fig 5: Anti-PvRBP2b mAbs inhibit reticulocyte binding and *P. vivax* invasion in Brazilian and Thai clinical isolates. (A) ELISA plates were coated with equimolar concentrations of each recombinant fragment and detection with anti-PvRBP2b mAbs 3E9, 6H1, 8G7 and 10B12 are shown. **(B)** Competition ELISA using immobilized PvRBP2b incubated with un-conjugated anti-2b mAbs (x-axis) and detected with 3E9-HRP, 6H1-HRP, 8G7-HRP and 10B12-HRP as indicated. For (A) and (B) error bars represent range showing the variability of duplicate measures. **(C)** $PvRBP2b_{161\text{-}1454}$ binding in the presence of anti-PvRBP2b mAbs 3E9, 6H1, 8G7 and 10B12 was analysed by flow cytometry. Normalized binding results where $PvRBP2b_{161\text{-}1454}$ binding in the absence of mAbs was arbitrarily assigned to be 100%. The anti-PvRBP2a mAb 3A11 was used as a negative antibody control. Mean ± S.E.M, n = 5, open dots represent biological replicates. The Kruskal-Wallis test was used to calculate the P value using 8G7 binding as no inhibition, *P ≤ 0.05, ***P ≤ 0.0001. **(D)** Invasion of *P. vivax* in Brazilian (blue open dots) and Thai (black open dots) clinical isolates in the presence of anti-PvRBP2b 3E9, 6H1, 8G7 and 10B12, pooled mAbs (each mAb at one third of final concentration), mouse isotype control, purified rabbit prebleed IgG, purified total IgG of anti-PvRBP2b polyclonal antibody R1527 and camelid anti-Fy6 mAb. Antibodies were added in concentrations from 25 μg/ml to 125 μg/ml except for the camelid anti-Fy6 mAb which was used at 25 μg/ml. Mean ± SD, n from 2 to 6, open dots represent biological replicates. For experiments with n > 2, we used the Kolmogorov-Smirnov test to compare 8G7 to 3E9, 6H1 and 10B12, *P ≤ 0.05, **P ≤ 0.001.

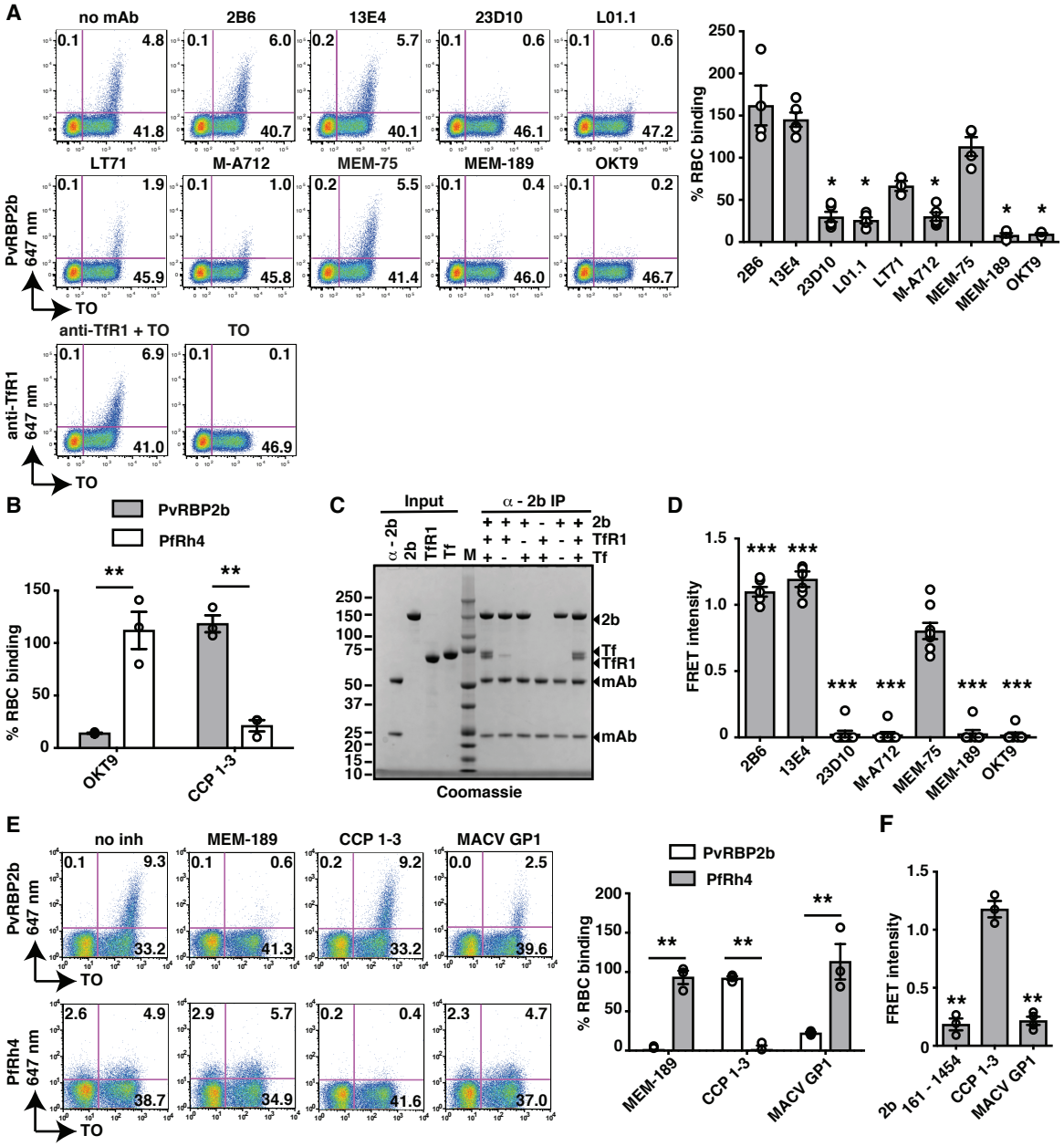
A
no mAb
2B6
13E4
23D10
L01.1
LT71
M-A712
MEM-75
MEM-189
OKT9
PvRBP2b 647 nm
TO
anti-TfR1 + TO
anti-TfR1 647 nm
% RBC binding
B
PvRBP2b
PfRh4
OKT9
CCP 1-3
C
Input
α - 2b IP
α - 2b
2b
TfR1
Tf
M
mAb
Coomassie
D
FRET intensity
E
no inh
MEM-189
CCP 1-3
MACV GP1
PfRh4 647 nm
F
2b
161 - 1454

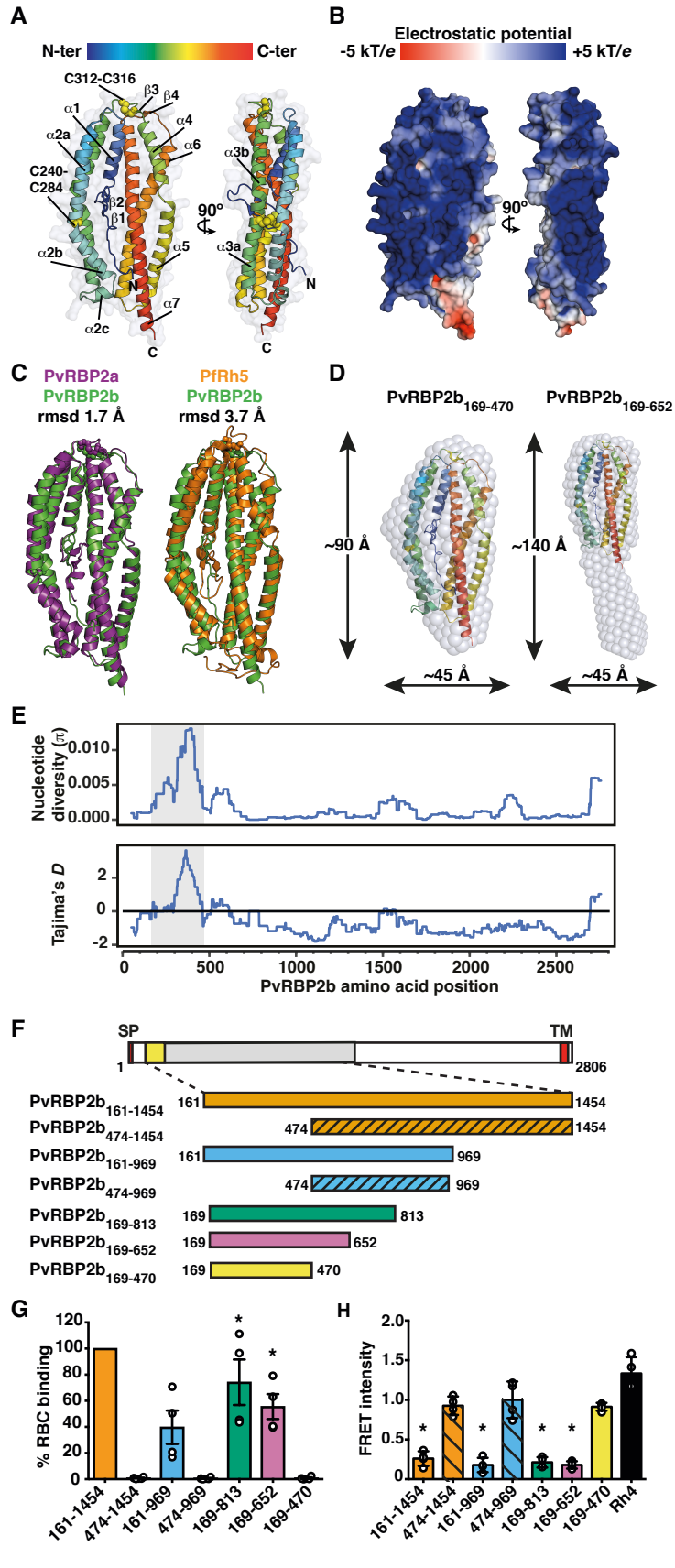
A
N-ter
C-ter
C312-C316
β3
β4
α1
α4
α2a
α6
C240-
C284
α3b
β2
β1
90°
α5
α3a
α2b
N
α7
α2c
C
B
Electrostatic potential
-5 kT/e
+5 kT/e
C
PvRBP2a
PvRBP2b
rmsd 1.7 Å
PfRh5
PvRBP2b
rmsd 3.7 Å
D
PvRBP2b169-470
PvRBP2b169-652
~90 Å
~140 Å
~45 Å
~45 Å
E
Nucleotide diversity (π)
0.010
0.005
0.000
Tajima's D
2
0
-2
0
500
1000
1500
2000
2500
PvRBP2b amino acid position
F
SP
TM
1
2806
PvRBP2b161-1454
161
1454
PvRBP2b474-1454
474
1454
PvRBP2b161-969
161
969
PvRBP2b474-969
474
969
PvRBP2b169-813
169
813
PvRBP2b169-652
169
652
PvRBP2b169-470
169
470
G
% RBC binding
120
100
80
60
40
20
0
161-1454
474-1454
161-969
474-969
169-813
169-652
169-470
H
FRET intensity
2.0
1.5
1.0
0.5
0
161-1454
474-1454
161-969
474-969
169-813
169-652
169-470
Rh4

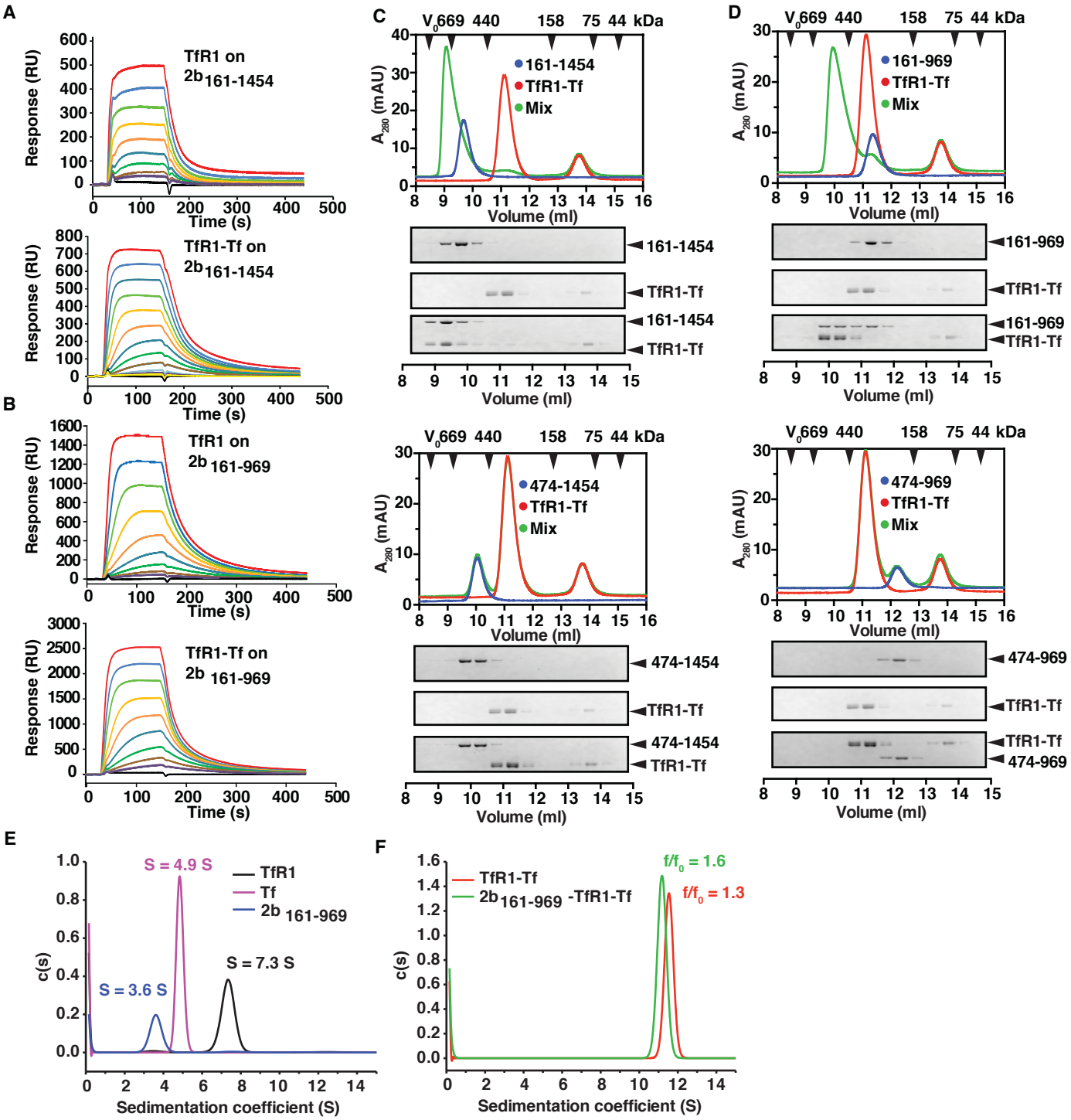
A
Response (RU)
TfR1 on
2b 161-1454
Time (s)
TfR1-Tf on
2b 161-1454
B
TfR1 on
2b 161-969
TfR1-Tf on
2b 161-969
C
V0 669 440 158 75 44 kDa
A280 (mAU)
161-1454
TfR1-Tf
Mix
Volume (ml)
161-1454
TfR1-Tf
D
161-969
474-1454
474-969
E
S = 4.9 S
S = 3.6 S
S = 7.3 S
TfR1
Tf
2b 161-969
c(s)
Sedimentation coefficient (S)
F
TfR1-Tf
2b 161-969 -TfR1-Tf
f/f0 = 1.6
f/f0 = 1.3

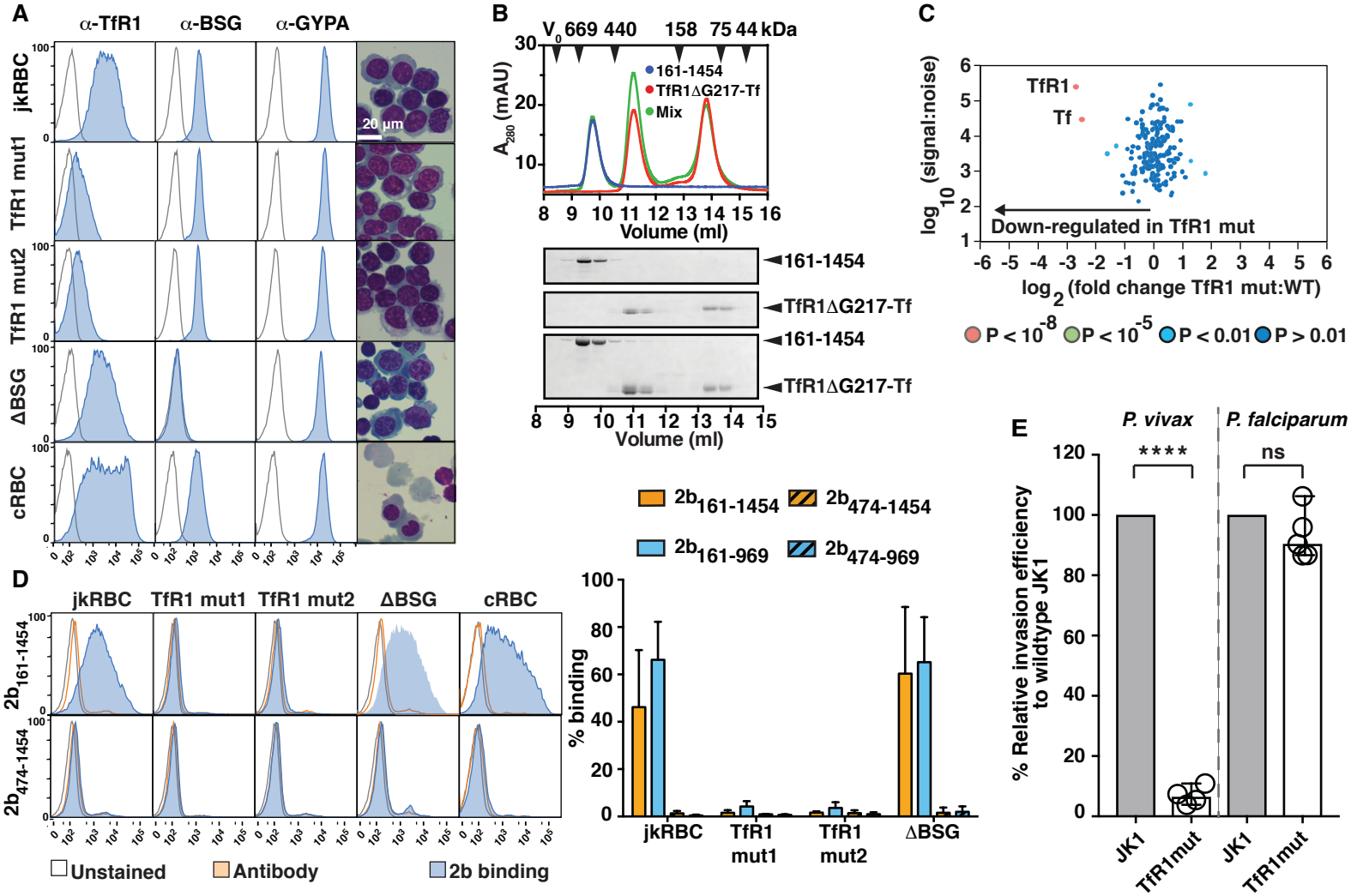
A
α-TfR1
α-BSG
α-GYPA
jkRBC
TfR1 mut1
TfR1 mut2
ΔBSG
cRBC
20 μm
B
V0 669 440 158 75 44 kDa
A280 (mAU)
161-1454
TfR1ΔG217-Tf
Mix
Volume (ml)
161-1454
TfR1ΔG217-Tf
161-1454
TfR1ΔG217-Tf
Volume (ml)
C
log10 (signal:noise)
TfR1
Tf
Down-regulated in TfR1 mut
log2 (fold change TfR1 mut:WT)
P < 10-8
P < 10-5
P < 0.01
P > 0.01
D
jkRBC
TfR1 mut1
TfR1 mut2
ΔBSG
cRBC
2b161-1454
2b474-1454
Unstained
Antibody
2b binding
2b161-1454
2b474-1454
2b161-969
2b474-969
% binding
jkRBC
TfR1 mut1
TfR1 mut2
ΔBSG
E
P. vivax
P. falciparum
****
ns
% Relative invasion efficiency to wildtype JK1
JK1
TfR1mut
JK1
TfR1mut

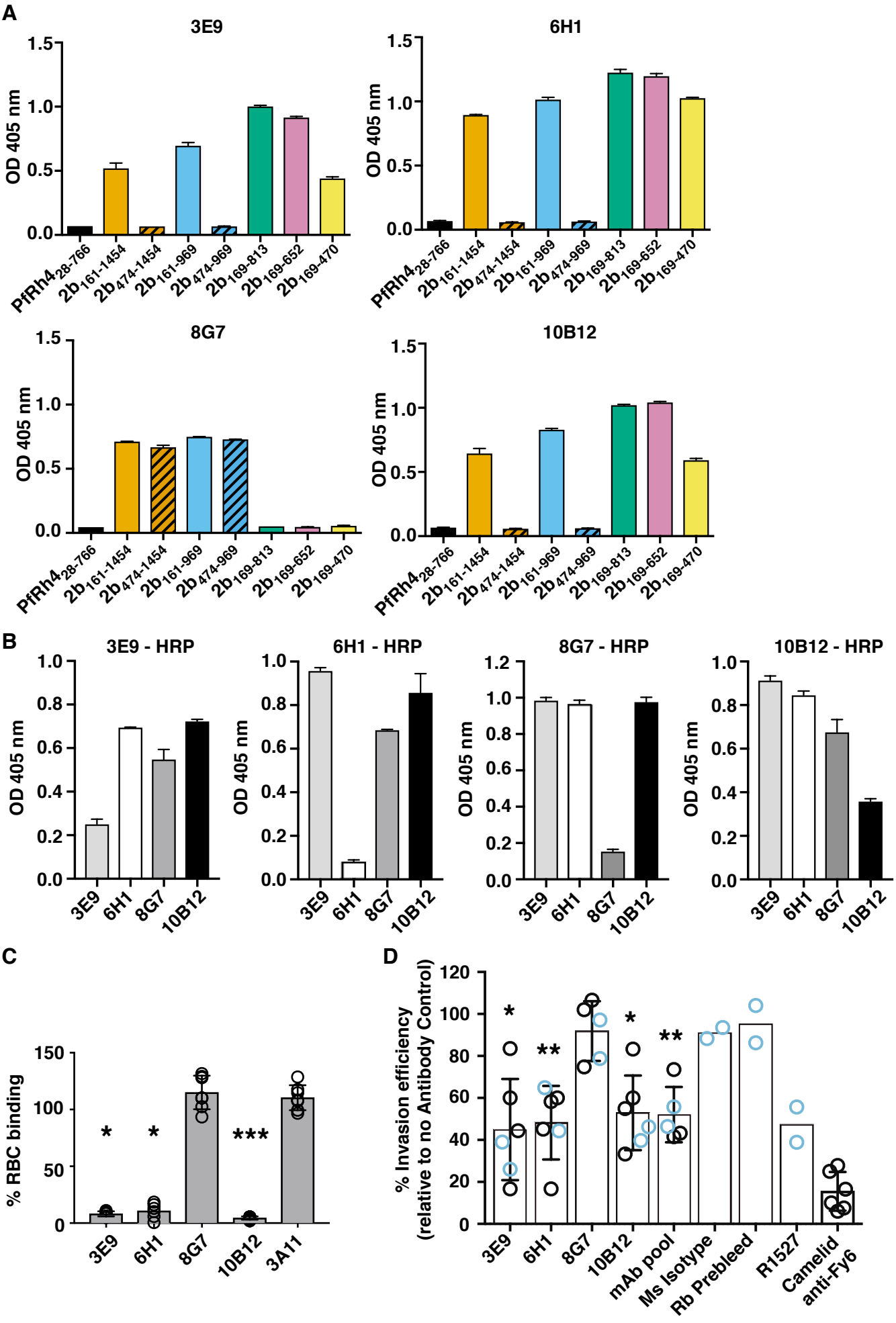
A
3E9
6H1
8G7
10B12
OD 405 nm
PfRh4 28-766
2b 161-1454
2b 474-1454
2b 161-969
2b 474-969
2b 169-813
2b 169-652
2b 169-470
B
3E9 - HRP
6H1 - HRP
8G7 - HRP
10B12 - HRP
C
% RBC binding
3A11
D
% Invasion efficiency (relative to no Antibody Control)
mAb pool
Ms Isotype
Rb Prebleed
R1527
Camelid anti-Fy6

Supplementary Materials for

Transferrin receptor 1 is a reticulocyte-specific receptor for *Plasmodium vivax*

Jakub Gruszczyk, Usheer Kanjee, Li-Jin Chan, Sébastien Menant, Benoit Malleret, Nicholas T.Y. Lim, Christoph Q. Schmidt, Yee-Foong Mok, Kai-Min Lin, Richard D. Pearson, Gabriel Rangel, Brian J. Smith, Melissa J. Call, Michael P. Weekes, Michael D. W. Griffin, James M. Murphy, Jonathan Abraham, Kanlaya Sriprawat, Maria J. Menezes, Marcelo U. Ferreira, Bruce Russell, Laurent Renia, Manoj T. Duraisingh, Wai-Hong Tham*

*Corresponding author: tham@wehi.edu.au

This PDF file includes:

Materials and Methods
Figs. S1 to S12
Tables S1 to S6
References (41-83)

Other Supplementary Material for this manuscript includes the following:

Dataset S1 as a separate Excel file

Materials and Methods

PvRBP2b cloning and sequencing

Sequence of PvRBP2b from *P. vivax* strain *Salvador I* was obtained from PlasmoDB Database (www.plasmodb.org; accession number: PVX_094255, total length 2,806 amino acids). Synthetic DNA was codon-optimized for expression in *E. coli* (Life Technologies). The sequence encompassing amino acids 161 to 1,454 of PvRBP2b was cloned into pMA-RQ (ampR) vector. Restriction free cloning was used to generate shorter fragments of the protein following a protocol described before (*41*). PvRBP2b sequence including residues 161 to 969 and 161 to 1,454 as well as the corresponding truncations: 474 to 969 and 474 to 1,454, were cloned into modified version of pET-32a(+) vector (Novagen) yielding constructs PvRBP2b$_{161\text{-}969}$, PvRBP2b$_{161\text{-}1454}$, PvRBP2b$_{474\text{-}969}$ and PvRBP2b$_{474\text{-}1454}$, respectively. These constructs allowed the expression of PvRBP2b proteins fused with bacterial thioredoxin, 6xHis-tag and tobacco etch virus (TEV) protease cleavage site at their N-termini. The TEV protease cleavage site enables removal of both tags. The construct used for crystallization, PvRBP2b$_{169\text{-}470}$ as well as PvRBP2b$_{169\text{-}652}$ and PvRBP2b$_{169\text{-}813}$ were cloned into pPROEX HTb vector and included N-terminal 6xHis-tag followed by a TEV cleavage site. All selected clones had their sequences verified at the Melbourne Translational Genomics Platform (MTGP). The list of all primer sequences used in this study is presented in Table S3 and a schematic representation of all PvRBP2b constructs is shown in Figure 2F.

Expression and purification of different variants of PvRBP2b

PvRBP2b$_{169\text{-}470}$ was expressed using *E. coli* strain SHuffle® T7 (New England Biolabs) and Terrific Broth (TB) supplemented with 100 μg/ml of carbenicillin. Flasks containing 1 liter of medium were incubated in Multitron shaker (Infors HT) at 37°C at 200 rpm. At OD_{600} of around 1.0, IPTG (Astral) was added to the final concentration of 1.0 mM and protein expression was allowed to continue for 20 hours at 16°C. Cells were harvested by centrifugation at 6,000 *x* g, resuspended in freezing buffer containing 50 mM TrisHCl pH 7.5, 500 mM NaCl, 10% (v/v) glycerol supplemented with cOmplete EDTA-free protease inhibitor cocktail (Roche), flash-frozen in liquid nitrogen and stored at -80°C until further processing.

For the purification cell pellet was thawed on ice and resuspended in the freezing buffer supplemented with 0.5 mg/ml of DNase and 1.0 mg/ml of lysozyme (both from Sigma-Aldrich). Cells were lysed using sonicator Sonopuls UW 3200 (Bandelin) equipped with VS 70 T probe. The obtained crude cell extract was clarified by centrifugation at 30,000 *x* g for 45 minutes at 4°C. The supernatant was applied on the 5 ml HisTrap column (GE Healthcare) pre-equilibrated with the freezing buffer. The unbound material was washed away using at least 10 column volumes of the washing buffer: 50 mM TrisHCl pH 7.5, 500 mM NaCl, 10% (v/v) glycerol and 10 mM imidazole. The bound protein was eluted from the column using the same buffer but containing 300 mM imidazole instead. The eluted fractions were pooled and dialyzed overnight in the presence of TEV protease into the buffer containing 20 mM NaHEPES pH 7.0 and 100 mM NaCl. The resulting protein sample was applied on the 5 ml SP-Sepharose HiTrap column (GE Healthcare) pre-equilibrated with the dialysis buffer. Unbound material was washed away using at least 10 column volumes of the buffer. The

protein was eluted from the column using the gradient of 20 mM NaHEPES pH 7.0 and 1.0 M NaCl. Collected fractions were analyzed on SDS PAGE and those containing the protein of interest were concentrated using Vivaspin 15 Turbo centrifugal concentrators (Sartorius) with a 5 kDa molecular weight cut-off and injected onto S75 Superdex 16/600 size exclusion column (GE Healthcare) pre-equilibrated with 20 mM NaHEPES pH 7.5 and 200 mM NaCl. The monodisperse peak fractions containing protein were pooled and concentrated using the same type of concentrator and used directly without freezing for the crystallization trials.

Expression and purification of two longer variants of PvRBP2b, PvRBP2b$_{161\text{-}969}$, PvRBP2b$_{161\text{-}1454}$ as well as truncations, PvRBP2b$_{169\text{-}652}$, PvRBP2b$_{169\text{-}813}$, PvRBP2b$_{474\text{-}969}$ and PvRBP2b$_{474\text{-}1454}$ were performed in a similar manner as described above or previously (*18*, *42*).

Cloning, expression and purification of recombinant PvRBPs

Proteins included in this study were PvRBP1a (amino acids [aa] 160–1,170), PvRBP1b (aa 140–1,275), PvRBP2a (aa 160–1,135), PvRBP2b (aa 161–1,454), PvRBP2cNB (aa 501–1,300) and PvRBP2-P2 (aa 161–641) Their expression and purification have been described previously (*18*, *19*, *42*).

Expression and purification of human transferrin receptor 1

A construct encoding the soluble ectodomain of human transferrin receptor 1 (TfR1, residues 121 to 760) was obtained from Addgene (pAcGP67A-TfR, Plasmid #12130, (*43*)). The TfR1 sequence follows a gene segment encoding the leader peptide from the baculovirus protein GP67, a 6xHis-tag, and a factor Xa cleavage site in a modified form of the pAcGP67A expression vector (Pharmingen) as described before (*43*). TfR1 was expressed in a lytic baculovirus/insect cell expression system using Sf21 cells (Life Technologies) and Insect-XPRESS™ Protein-free Insect Cell Medium supplemented with L-glutamine (Lonza). Protein expression was induced by inoculation of the cell culture at around 1 x 10^6 cells/ml with the third passage stock (P3) of virus and typically allowed to progress for three days. Media supernatant was separated from the cells by centrifugation at 2,000 *x* g for 20 min and concentrated until around 10% (v/v) of their initial volume using tangential flow filtration device equipped in a cassette with 10 kDa molecular weight cut-off (Millipore).

Concentrated supernatants were subsequently dialyzed into a buffer containing 20 mM TrisHCl pH 7.5 and 300 mM NaCl in order to remove the residuals of the culture media that might interfere with the subsequent steps of purification. After dialysis, protein was captured from the solution using Ni-NTA chromatography. The dialyzed sample was loaded onto 5 ml HisTrap column (GE Healthcare) pre-equilibrated with the dialysis buffer. Unbound material was washed away with at least 10 column volumes of the same buffer supplemented with 20 mM imidazole. Protein was eluted from the column with 300 mM imidazole in the dialysis buffer. Obtained sample was concentrated using Vivaspin 15 Turbo centrifugal concentrators (Sartorius) with a 5 kDa molecular weight cut-off and injected onto S200 Superdex 16/600 size exclusion column (GE Healthcare) pre-equilibrated with a buffer containing 20 mM NaHEPES pH 7.5, 100 mM NaCl and 50 mM $NaHCO_3$. The final samples were supplemented with 10% (v/v) glycerol, flash-frozen in liquid nitrogen and stored at -80°C.

Expression and purification of TfR1 mutant ΔG217

Synthetic DNA corresponding to the sequence of human TfR1 (residues 121 to 760) and harboring a Gly217 deletion was ordered from Life Technologies. The gene was multiplied using PCR and primers introducing BamHI and NotI restriction sites on its ends. The PCR product was digested with the corresponding restriction enzymes and ligated into pAcGP67A vector previously digested with the same enzymes. The sequence of the obtained clone was verified using Melbourne Translational Genomics Platform. The sequence of the obtained clone was identical with the wild-type except the introduced ΔG217 mutation. Expression and purification of the mutant protein were performed as described above for the wild-type TfR1 protein.

Purification of human transferrin

Apo-transferrin purified from human serum was purchased from Sigma-Aldrich (Catalog Number T4382). The protein powder was resuspended in a buffer containing 100 mM disodium carbonate at pH 5.9. Loading of transferrin with iron was performed as described in the manufacturer's leaflet by adding a solution of ferrous ammonium sulfate, hexahydrate (Sigma-Aldrich) corresponding to 2% (w/w) of protein mass. The sample was incubated with stirring for one hour at room temperature. The pH was then raised to 8.5 using 1.0 M disodium carbonate and the solution was mixed for the additional two hours. Holo-transferrin was subsequently re-purified by gel filtration chromatography using a S200 Superdex 16/600 size exclusion column (GE Healthcare) equilibrated with 20 mM NaHEPES pH 7.5, 100 mM NaCl and 50 mM $NaHCO_3$ buffer. The final samples were supplemented with 10% (v/v) glycerol, flash-frozen in liquid nitrogen and stored at -80°C.

MACV GP1 cloning, expression and purification

MACV GP1 (Carvallo strain, residues 87-240) along with an N-terminal 6xHis-tag, a TEV protease site, and a short linker (amino acids SGSG) was subcloned into the pHLsec vector (*44*). The protein was produced by transfection using linear polyethylenimine in GnTI-/- 293S cells grown in suspension and then purified using nickel affinity purification followed by reverse nickel affinity purification and size-exclusion chromatography on a Superdex 200 column.

Calculation of protein concentration

Molecular weights and extinction coefficients for different variants of PvRBP2b protein were calculated using ProtParam from ExPASy server (http://web.expasy.org/protparam/). Molecular weights for transferrin and transferrin receptor 1 were obtained experimentally using Mass Spectrometry (MS) and their extinction coefficients were found in the literature (*43*, *45*). All the values are presented in Table S4.

TfR1-Tf and PvRBP2b$_{161-969}$-TfR1-Tf complex formation

The binary complex between Tf and TfR1 was created by mixing equimolar amounts of proteins and incubating them overnight at 4°C. The complex was subsequently re-purified by gel filtration chromatography using a S200 Superdex 16/600 size exclusion column (GE Healthcare) equilibrated with 20 mM NaHEPES pH 7.5, 100

mM NaCl and 50 mM $NaHCO_3$ buffer. The ternary complex between $PvRBP2b_{161-969}$ and TfR1-Tf was created in an analogical way.

Antibodies

Anti-PvRBP polyclonal antibodies production was performed at the Walter and Eliza Hall Institute Monoclonal Antibody Facility (*19*). Rabbits were immunized five times with 150 μg of $PvRBP2b_{161-1454}$. The first immunization was administered with Complete Freund's adjuvant and the rest with Incomplete Freund's Adjuvant. Rabbit IgG were purified from serum using Protein G sepharose.

All anti-PvRBP mAbs were produced at the Monoclonal Antibody Facility at the Walter and Eliza Hall Institute. BALB/c and C57Bl6 mice received three immunizations of recombinant $PvRBP2b_{161-1454}$. At day 0, Complete Freunds adjuvant was mixed with the antigen into an emulsion and injected intra-peritoneally. At day 30, and day 60, the antigen was mixed with incomplete Freunds adjuvant, and the emulsion injected intra-peritoneally. Serum ELISA titrations were performed at day 72. The mouse with the best response received a final injection of antigen in saline, and splenocytes were harvested three days later. Spleen cells were fused with SP2/0 myeloma cells to form B-cell-myeloma fused cells (hybridomas). Hybridomas were grown in hypoxanthine-aminopterine thymidine growth medium. ELISA was used to select hybridomas producing antibodies specific to the immunized antigen. Hybridomas were cloned by limiting dilution in multi-well plates aiming for one cell or less per well. The sub-cloning supernatants were screened by ELISA. Two or more rounds of limiting dilution cloning were generally required before the hybridomas were deemed monoclonal. The antibodies were purified from monoclonal hybridoma supernatants with protein A sepharose.

Anti-TfR1 antibodies were obtained from the following suppliers: MEM-75 (ab9179), 2B6 (ab38168), 23D10 (ab10251), LT71 (ab38446) and 13E4 (ab38171) from Abcam, OKT9 from Stemcell Technologies (60106), L01.1 (347510) and M-A712 (555534) from BD Biosciences. For surface staining in Fig. 4A and Fig. S1A, we used the following antibodies anti-TfR1/CD71-APC (M-A712,1:20, BD Pharmigen 551374), anti-CR1/CD35-Alexa647 (E11, 1:100, BD Pharmigen 565329), GlyA-PE-Cy5 (JC159, 1:1000, Abcam ab201309), anti-Basigin/CD147-APC (VJI/9, 1:20, Abcam ab91150), anti-DARC/CD234-APC (*REA376*, 1:100, Miltenyi Biotec 130105684) and anti-DAF/CD55-PE-Cy5 (143-30, 1:100, Abcam ab25410).

Reticulocyte enrichment for flow cytometry-based red blood binding

500 ml of whole blood (Australian Red Cross) was passed through a RC high efficiency leucocyte removal filter (Haemonetics Australia) and washed three times with phosphate-buffered saline buffer (PBS) at 2,000 *x* g for five minutes to remove the serum component. Red blood cells were adjusted to approximately 50% haematocrit with PBS and 5.5 ml was carefully layered on 6 ml of 70% (v/v) isotonic Percoll cushion (GE Healthcare). After centrifugation at 2,000 *x* g for 25 minutes, a thin band of enriched reticulocytes at the Percoll interface was collected. Reticulocytes were stored in RPMI wash buffer (Gibco) at 4°C until further usage.

Enzymatic treatment of red blood cells

Red blood cells were treated with trypsin (Sigma-Aldrich), chymotrypsin (Worthington) and neuraminidase (Sigma-Aldrich). 480 µl of packed blood was washed with 12 ml of wash buffer (RPMI HEPES medium with 25 mM $NaHCO_3$), spun down at 2,000 *x* g for one minute and resuspended in 12 ml of wash buffer. 2 ml of the resuspension was used for each sample (i.e. untreated, high trypsin, low trypsin, chymotrypsin and neuraminidase). Samples were spun down at 2,000 *x* g for 1 minute and the wash buffer was removed. Packed blood (~80 µl) was treated with 2 ml of the various enzymes at the following concentrations, high trypsin (1 mg/ml), low trypsin (0.1 mg/ml), chymotrypsin (1 mg/ml) and neuraminidase (0.07 U/ml). Samples were incubated at 37°C for 1 hour and washed with 4 ml of wash buffer. Wash buffer was replaced with 1 ml of chymotrypsin/trypsin inhibitor (Worthington) at 1 mg/ml and incubated for 10 minutes. Samples were washed and stored in 4 ml of wash buffer at 4°C.

Flow cytometry-based red blood cell binding assay

Reticulocyte preparations were resuspended in PBS to a final a final volume of 1 x 10^7 cells/ml. Recombinant proteins were incubated at 0.01 mg/ml in 100 µl of the resuspended reticulocyte population for an hour at room temperature. All washes were performed in PBS supplemented with 1% (w/v) bovine serum albumin (BSA) and spun at 4,000 *x* g for 1 minute and all antibody incubations were performed at room temperature for one hour. The binding assays were washed once and incubated with the respective rabbit polyclonal antibodies (12.5 µg/ml). After washing, Alexa Fluor 647 chicken anti-rabbit secondary antibody (1:100; Life Technologies) was added. After a final wash, 100 µl thiazole orange (TO) (Retic-Count Reagent; BD Biosciences) was added and incubated for half an hour. The TO stain was removed and red blood cells were resuspended in 200 µl PBS and analysed on the FACSCalibur flow cytometer (BD Biosciences). 50,000 events were recorded and results were analysed using FlowJo software (Three Star). The background signal from a rabbit polyclonal antibody and Alexa Fluor 647 conjugated antibody control (without protein) was subtracted from all binding results. To enable comparison between biological repeats, percentage binding of the protein in the presence of inhibitors/mAbs was divided by the percentage binding with no inhibitor/no mAbs and multiplied by 100 to get the percentage binding relative to the no inhibitor control. For our inhibition studies, anti-TfR1 antibodies were added at 0.05 mg/ml, MACV GP1 at 0.5 mg/ml and CCP 1-3 at 0.3 mg/ml.

Immunoprecipitation experiments

Immunoprecipitation assays were performed using 0.25 mg/ml of both $PvRBP2b_{161-1454}$ and TfR1-Tf complex and 0.05 mg/ml of anti-PvRBP2b mAb in 100 µl reaction volume in PBS. After one hour incubation at 4°C on rollers, 10 µl of packed Protein G-sepharose beads was added to bind anti-PvRBP2b mAbs and incubated overnight at 4°C on rollers. Beads were washed three times in PBS and spun down at 2,000 *x* g for two minutes. Anti-PvRBP2b mAbs and associated proteins were eluted from beads by boiling for five minutes in 2x SDS-PAGE reducing sample buffer and analysed on 4-12% Bis-Tris gels (Invitrogen). Protein bands were visualized by staining with SimplyBlue SafeStain (Life Technologies).

Fluorescence resonance energy transfer (FRET) assay

PvRBP2b$_{161\text{-}1454}$ and TfR1 were labelled with N-hydroxysuccinimide ester-activated DyLight 488 (DL488) and DyLight 594 (DL594) (Life Technologies) respectively. The dyes were dissolved in dimethyl sulfoxide (DMSO) (Sigma) and added at five-fold molar excess to the protein being labelled. After one hour incubation at room temperature, un-conjugated dye removed using a Micro Bio-Spin P-6 column (BioRad) at 1,000 *x* g for two minutes. Average dye per protein was ~3.5 dye/protein for PvRBP2b$_{161\text{-}1454}$ and ~1.8 dye/protein for TfR1. PvRBP2b$_{161\text{-}1454}$-DL488, TfR1-DL594 and Tf were mixed in a 1:1:1 molar ratio with excess of candidate inhibitor in a final 10 µl of reaction volume in FRET buffer read in 384-well plates (Corning). One µl of 1% (w/v) SDS was added to one well to measure background signal. Fluorescence intensity was measured using EnVision plate reader (PerkinElmer Life Sciences). DL488 (donor) fluorescence was measured with a 485/14-nm excitation filter and 535/25-nm emission filter and DL594 (acceptor) fluorescence was measured with a 590/20-nm excitation filter and 615/9-nm emission filter. Sensitized emission was measured with a 485/14-nm excitation filter and 615/9-nm emission filter.

Generation of TfR1 mutant JK-1 cells

The erythroleukemia cell line JK1 was used to generate CRISPR/Cas9-based deletions of *TFRC* (*46*). Briefly, JK1 cells were maintained in an undifferentiated state in JK1 growth media: Iscove's Modified Dulbecco's Medium (IMDM) with Glutamax (ThermoFisher), 0.5% (v/v) penicillin/streptomycin (ThermoFisher), 10% AB+ octoplasLG (OctoPharma), 2 IU/ml heparin (Affymetrix) and 10 µM tranylcypromine (Cayman Chemicals). Cells were transduced with a lentivirus containing the Cas9 expression plasmid LentiCas9-Blast (*47*) and selected for with 6 µg/ml blasticidin (Sigma-Aldrich) to produce JK-1-Cas9. GuideRNAs (sgRNAs) targeting *TFRC* were identified using the Broad Institute Genetic Perturbation Platform sgRNA designer tool (*48*) and the four top gRNAs were selected: TFRC-g1 (Broad ID: TFRC_196074043_s) 5′-CAGGAACCGAGTCTCCAGTG; TFRC-g2 (Broad ID: TFRC_196072124_s) 5′-AAATTCATATGTCCCTCGTG; TFRC-g3 (Broad ID: TFRC_196071432_as) 5′-GGGGGTTATGTGGCGTATAG; TFRC-g4 (Broad ID: TFRC_196068088_s) 5′-AATTGGTGTGTTGATATACA. The sgRNA sequences were cloned into LentiGuide-Puro (*47*) following which lentivirus containing the vector was produced (*49*). The lentivirus was transduced into the JK-1-Cas9 line and the cells were selected on both blasticidin and 2 µg/ml puromycin (Sigma-Aldrich).

Expression of TfR1 on the transduced cells was monitored by flow cytometry using a Milteny MACSQuant instrument with 405 nm, 488 nm and 638 nm lasers (Miltenyi Biotec), following staining with a 1 in 20 dilution of α-TfR1-APC (Miltenyi Biotech, San Diego, CA) for 30 minutes at room temperature in PBS + 0.5% BSA. Within 2-3 weeks post transduction, a TfR1-negative population was observed only with the TFRC-g3 sgRNA. Single cell clones were obtained by limiting dilution and the CRISPR/Cas9 target region was PCR amplified using the following primers: TFRC-g3-F 5′-GGTAAATTTCCTCAAGCCAAA and TFRC-g3-RC 5′-CAGGACATGGGGAAAGTGAT. The size and location of the indel was determined by Tracking of Indels by Decomposition (TIDE) analysis (*50*). Two clones (TfR1 mut1 and TfR1 mut 2) were used for subsequent experiments.

Induction of jkRBCs for TfR1 binding studies

Wild-type and mutant (TfR1 mut1 and TfR1 mut2) cell lines were induced to differentiate using epigenetic factor PFI-1. Briefly, cells were expanded in JK-1 growth media and to start induction cells were washed and resuspended in JK1 differentiation media: Iscove's Modified Dulbecco's Medium (IMDM) with Glutamax (ThermoFisher), 0.5% (v/v) penicillin/streptomycin (ThermoFisher), 10% AB+ octoplasLG (OctoPharma), 2 IU/ml heparin (Affymetrix), 330 µg/ml human holotransferrin (Scipac) and 2 µM PFI-1 (Cayman Chemicals). Cells were differentiated for between 12-14 days and media changes were made every 4-5 days. Differentiation into jkRBCs was validated by staining for GypA with a 1 in 100 α-GypA-FITC (StemCell Technologies) and BSG with 1 in 100 α-BSG-FITC (Thermo Fisher Scientific, USA), followed by flow cytometry. Cytospins were prepared as described (*51*).

Quantitative surface proteomics

We adapted our previously described method (*51*, *52*). Briefly, 2×10^7 of each cell type were washed with PBS and then surface sialic acid residues were chemically biotinylated following oxidation with sodium meta-periodate (Thermo) and reaction with aminooxy-biotin (Biotium). After quenching the reaction with 5 mM glycerol in PBS (Sigma-Aldrich), cells were incubated in Triton X-100 lysis buffer. Streptavidin agarose beads (Pierce) were used to enrich for biotinylated glycoproteins, and after extensive washing, the captured proteins were denatured with dithiothreitol (Sigma-Aldrich), alkylated with iodoacetamide (IAA, Sigma) and digested on-bead with trypsin (Promega) in 200 mM sodium HEPES pH 8.5 for 3 hours. The tryptic peptides were recovered and labeled with tandem mass tag (TMT) reagents (*52*). Following quenching with hydroxylamine, the TMT-labeled samples were combined in a 1:1:1:1 ratio, enriched and desalted and then 75% of the total sample was separated into 6 fractions using tip-based strong cation exchange columns (*52*). Of the remaining 25% of the total sample, a portion (10% of total sample) was subject to mass spectrometry unfractionated.

Mass spectrometry data was acquired using an Orbitrap Fusion coupled with a UltiMate 3000 Nano LC (Thermo Fisher Scientific). Peptides were separated using a 90 min linear gradient of 3 to 33% (v/v) acetonitrile in 0.1% formic acid at a flow rate of 200 nl/min (fractionated samples) or a 180 min gradient with otherwise identical parameters (unfractionated sample), and the separation was done on a 75 cm PepMap C18 column (Thermo Fisher Scientific). Each analysis used a MultiNotch MS3-based TMT method (*52*, *53*). The scan sequence began with an MS1 spectrum (Orbitrap analysis, resolution 120,000, 400-1400 Th, AGC target 2×10^5, maximum injection time 50 ms). MS2 analysis consisted of CID (quadrupole ion trap analysis, AGC 15,000, NCE 35, maximum injection time 120 ms). The top ten precursors were selected for MS3 analysis, in which precursors were fragmented by HCD prior to Orbitrap analysis (NCE 55, max AGC 2×10^5, maximum injection time 150 ms, isolation specificity 0.5 Th, resolution 60,000). A Sequest-based in house software pipeline was used to process mass spectra as previously described (*52*). The human Uniprot database (April 2014) was used to search for proteins and samples were concatenated with common contaminants (*52*) and filtered to a final protein-level false discovery rate of 1%. In order to compare signals between different TMT channels, TMT reporter ion counts across all peptide-spectral

matches were summed using in-house software as previously described (*52*). Poor quality MS3 spectra with a combined signal:noise ratio < 250 across all TMT reporter ions were excluded. For protein quantitation, reverse and contaminant proteins were removed, then each reporter ion channel was summed across all quantified proteins and normalized assuming equal protein loading across all samples. Fold change for each protein was calculated according to (average signal:noise (TfR1 mutants) / average signal:noise (JK-1 controls). Protein quantitation values were exported for further analysis in Excel. Gene Ontology Cellular Compartment terms were downloaded from www.uniprot.org and p-values (Significance A) calculated and adjusted with the Benjamini Hochberg method using Perseus version 1.2.0.16 (*54*).

Crystallization of PvRBP2b$_{169\text{-}470}$

Crystallization screens were set up at the Collaborative Crystallization Center in Parkville using crystallization robot Phoenix (Art Robbins Instruments) and sitting drop vapor diffusion method in 96-well format plates. 150 nl of protein sample at two different concentrations, 7.5 and 15.0 mg/ml, were mixed with the reservoir in 1:1 ratio. Two different sparse matrix screens were set up covering wide range of different crystallization conditions. Plates were incubated at 20°C and drops were monitored regularly over the period of 3 months. First crystals appeared after 24 hours in the condition containing 20% (w/v) PEG 3,350, 200 mM potassium thiocyanate and 100 mM Bis-Tris pH 7.5. The initial crystal hit was optimized manually using the hanging drop method, 24-well Linbro plates (Hampton Research) and varying pH and PEG concentration. For data collection crystals were cryo-protected in a reservoir solution supplemented with 20% (v/v) glycerol and frozen in liquid nitrogen.

X-ray diffraction data collection and structure determination

Diffraction data were collected at MX2 microfocus beamline at the Australian Synchrotron Facility in Clayton at 0.9537 Å wavelength using ADSC Quantum 315r detector. The best crystal diffracted to 1.71Å resolution and belonged to the primitive monoclinic space group $P2_1$ with cell dimensions a = 59.50 Å, b = 124.20 Å, c = 65.31 Å, α = 90.00°, β = 97.75° and γ = 90.00°. The collected diffraction data were integrated using iMosflm (*55*). Scaling and merging were performed using program Aimless from the CCP4 package (*56*). The cell content was analyzed using program Matthews (*57*). Molecular replacement was attempted using Phaser (*58*) and PvRBP2a as a model (PDB accession number 4Z8N). The search yielded a definitive solution containing two molecules in the asymmetric unit. The initial model was rebuilt automatically using program AutoBuild (*59*) followed by a manual improvement using program Coot (*60*). The structure was refined using the program Phenix Refine (*59*) and including TLS that were generated using TLSMD web server (*61*). Multiple cycles of model building and atomic refinement yielded a structure that was eventually refined to 1.71 Å resolution with the final R_{work} = 0.168 and R_{free} = 0.188. The refinement statistics are given in Table S1. The atomic coordinates and structure factors have been deposited in Protein Data Bank with accession number 5W53.

Analytical size exclusion chromatography (SEC)

Analytical chromatography was performed at room temperature using ÄKTA pure 25 M1 chromatographic system (GE Healthcare). Proteins were separated alone as well as mixed in all possible combinations. In order to facilitate the analysis, proteins were mixed in equimolar ratio and the same amount of given protein was used throughout the experiment. Samples were incubated for 1 hour to allow complex formation and then 100 µl were injected onto Superdex 200 Increase 10/300 GL column (GE Healthcare) equilibrated with 20 mM NaHEPES pH 7.5, 100 mM NaCl, 50 mM $NaHCO_3$ at 0.75 ml/min of buffer flow. The absorbance of the eluent was monitored at 280 nm. The eluate was collected in 0.5 ml fractions. Obtained fractions were analyzed using SDS PAGE. The column was calibrated with high- and mid-mass molecular mass markers (GE Healthcare) as described in the manufacturer's instructions. The results of the calibration are shown in Figure S5.

Surface plasmon resonance (SPR) data collection, processing and analysis

All experiments were carried out at 25°C using a Reichert SR7500DC SPR instrument (Reichert Technologies, Buffalo, NY) using the integrated SPR autolink software package. Data analysis was performed using the TraceDrawer software package (Ridgeview Instruments AB). The running buffer consisted of 20 mM NaHEPES at pH 7.5 including 100 mM NaCl, 50 mM $NaHCO_3$ and 0.005% (v/v) Tween 20 and was used for the SPR experiments that probe the interactions with TfR1. To analyze the interactions of TfR1 and TfR1-Tf complexes with PvRBP2b, 4,300 RUs of the fragment $PvRBP2b_{161-969}$ or 1,300 RUs of the fragment $PvRBP2b_{161-1454}$ were covalently fixed to a carboxymethyldextran hydrogel biosensor chip (CMD500m, purchased from XanTec Bioanalytics, Duesseldorf, Germany) using standard amine coupling according to the manufacturer's instructions. The reference surface was blank immobilized. To probe binding, a concentration series of TfR1 or TfR1-Tf complexes was injected (as indicated) at 25 µl/min for 2 min followed by buffer flow for 5 min and a regeneration step consisting of an injection of 1.0 M NaCl for 30 s. The TfR1 concentration of 7.5 nM or the 7.5:15 nM mixture of the TfR1-Tf complex was injected twice to assess reproducibility. Reference subtracted sensorgrams of two-fold dilution series are shown. For Fig. 3A, 1,300 RUs of $PvRBP2b_{161-1454}$ were coupled covalently to a carboxymethyldextran hydrogel biosensor chip to probe binding of TfR1 and TfR1:Tf complexes. Soluble TfR1 was assayed in a concentration range from 2 µM to 7.5 nM, whereas soluble TfR1:Tf complexes were assayed in a range from 2 µM:4 µM to 1.8 nM:3.9 nM. For Fig. 3B, 4,300 RUs of $PvRBP2b_{161-969}$ were coupled covalently to a carboxymethyldextran hydrogel biosensor chip. Soluble TfR1 binding is shown for a concentration series ranging from 2 µM to 7.5 nM and the concentration range of TfR:Tf complexes range from 2 µM:4 µM to 7.5 nM:15 nM.

To probe the interaction with anti-PvRBP2b monoclonal antibodies (mAbs) $PvRBP2b_{161-1454}$ was immobilised via standard amine coupling onto carboxymethyldextran sensorchips (CMD500m, Xantec bioanalytics) and 3E9, 6H1 and 10B12 mAbs were flown over the surfaces at the concentrations 40, 52 and 40 nM, respectively. As running buffer, 10 mM NaHEPES pH 7.4 with 150 mM NaCl, and 0.005% (v/v) Tween 20 was used throughout. The antibodies 3E9 and 10B12 were analysed on a single $PvRBP2b_{161-1454}$ surface with 10,000 RU of the protein being coated.

Apart for 10B12 extensive buffer flow of up to 12 h in between cycles was sufficient to substantially dissociate the antibody-PvRBP2b complexes. The 6H1 mAb was assayed on another CMD500 chip coated with 1,300 RU of $PvRBP2b_{161-1454}$. The binding curves were fit to a bivalent (2:1) interaction model using the TRACEDRAWER software package to estimate affinity constants for the bivalent interaction. Table S6 summarizes the corresponding kinetic parameters (k_a and k_d), the equilibrium dissociation constants (K_{D1} and K_{D2}) and the χ^2 values of goodness of the fit.

Small angle X-ray scattering (SAXS) data collection, processing and analysis

SAXS data were collected on the SAXS/WAXS beamline at the Australian Synchrotron using the inline size-exclusion chromatography setup and processed as described previously (*62*). 2D scattering data were radially averaged, normalized to sample transmission and an average of background scattering profiles was subtracted using the ScatterBrain software (written by Stephen Mudie, Australian Synchrotron). The ATSAS suite of software was used for all subsequent SAXS data analyses. For an initial assessment of data quality, Guinier analysis was performed using PRIMUS (*63*). The program GNOM (*64*) applied an indirect Fourier transform to the scattering profile to calculate the pair-wise intra-atomic distance distribution function $P(r)$ and D_{max}, the maximum dimension of the particle. Theoretical scattering curves were calculated from atomic coordinates and compared with experimental scattering curves by using CRYSOL (*65*). Low-resolution shape envelope was generated with the *ab initio* bead-modeling program DAMMIF (*66*), by performing 20 independent reconstructions, aligning all with the most probable model with DAMSEL and DAMSUP, averaging models with DAMAVER and adjusting to correspond with the experimentally determined excluded volume with DAMFILT (*67*).

The crystal structure of $PvRBP2b_{169-470}$ was fitted into the obtained SAXS envelope using rigid-body search and program COLORES (*68*). The program returned four individual models that were subsequently judged based on the value of the correlation coefficient given for each model as well as the agreement with the available biological information (sequence of the residues constituting the protein fragment and the predicted direction of the polypeptide chain). The results of the superimposition were visualized using PyMOL (*69*). The data collection and processing statistics are presented in Table S2.

Analytical ultracentrifugation (AUC) data collection, processing and analysis

Samples were analysed using an XL-I analytical ultracentrifuge (Beckman Coulter, Fullerton, CA) equipped with an AnTi-60 rotor. Radial absorbance data were acquired at 20°C using a rotor speed of 50,000 rpm (201,600 *x* g) and a wavelength of 280 nm, with radial increments of 0.003 cm. The sedimenting boundaries were fitted to to a continuous sedimentation coefficient distribution [$c(s)$] model with SEDFIT (*70*), using a regularization parameter of p = 0.95, floating frictional ratios, and 250 sedimentation coefficient increments in the range of 0-20 S. The partial specific volumes of proteins, buffer density, and buffer viscosity were calculated using SEDNTERP (*71*).

Circular dichroism (CD) data collection, processing and analysis

CD data were collected using circular dichroism spectrometer Model 410 (Aviv Biomedical) and analyzed as described before (*18*). Before the experiment, protein samples were dialyzed extensively overnight into 20 mM NaHEPES pH 7.5, 100 mM NaCl, 50 mM $NaHCO_3$ buffer. For the measurements, the protein concentration was set to 3.0 µM. The CD spectra were recorded between 260 and 190 nm with 1 nm wavelength step and 4 s averaging time at 25°C. 120 µl of the protein sample was using quartz cell (Hellma) with the optical path of 0.05 cm. After subtracting the background from the buffer the spectra were processed using DichroWeb server (*72*, *73*). The experimental data were converted to mean residue molar ellipticity (θ). The content of secondary structures was predicted using CDSSTR algorithm (*74*) and SMP180 reference set (*75*) for 190-240 nm.

Secondary structures predictions

Secondary structures predictions for PvRBP2b were performed using JNet Secondary Structure Prediction algorithm integrated into Jalview 2.10.1 (*76*).

Population genetic analyses

We downloaded genotype data from https://www.malariagen.net/data/p-vivax-genome-variation-may-2016-data-release and extracted variants from the coding region of PvRBP2b using bcftools 1.3.1. We converted the VCF to a diploid VCF (changing 0 and 1 to 0/0 and 1/1 respectively) using sed commands. We calculated nucleotide diversity and Tajima's *D* using scikit-allel 1.1.8. To give the most accurate estimate of true diversity we used all SNPs discovered within the gene, including those that failed variant filters. Code used can be found at https://github.com/podpearson/PvRBP2b/blob/master/20170803_RBP2b_diversity_for_Wai-Hong.ipynb

Detection of PvRBPs and PfRh4 by polyclonal and monoclonal antibodies by ELISA

96-well flat-bottomed plates (Maxisorp; Nunc) were coated with 65 nM of recombinant PvRBP1a, PvRBP1b, PvRBP2a, PvRBP2b, PvRBP2cNB, PvRBP2-P2 or PfRh4 fragments in 100 ul of PBS at 4°C overnight. All washes were done three times using PBS/0.1% Tween and all protein and antibody incubations were performed for one hour at room temperature. Coated plates were washed and blocked with 10% (w/v) skim milk solution (Devondale) for one hour at room temperature. After blocking, primary monoclonal or polyclonal antibodies were added (0.001 µg/µl), washed and subsequently incubated with horseradish peroxidase (HRP)-conjugated rabbit anti-mouse or HRP-conjugated goat anti-rabbit secondary antibody (1:1000 or 1:200 respectively; Fisher Scientific). The primary mAbs were against PvRBP1a (4E3), PvRBP1b (4G4), PvRBP2a (3A11), PvRBP2b (3E9, 6H1, 8G7 and 10B12), PvRBP2cNB (6H2), PvRBP2-P2 (9E3) and PfRh4 (10C9). Plates were washed twice with PBS/0.1% Tween and a final wash with PBS to remove residual Tween. 100 µl of azino-bis-3-ethylbenthiazoline-6-sulfonic acid (ABTS liquid substrate; Sigma) was added and incubated in the dark at room temperature for approximately three minutes. 100 µl of 1% (w/v) SDS was used to stop the reaction. Absorbance was read at 405 nm and all samples were performed in duplicate.

P. vivax ex vivo invasion assay

In general, the *ex vivo* assays using Thai and Brazilian isolates were performed by incubating mature parasites with TfR1-positive enriched reticulocytes in either the absence or in the presence of up to 125 μg/ml of anti-PvRBP2b mAbs 3E9, 6H1, 8G7 and 10B12, 125 μg/ml pooled anti-PvRBP2b mAbs (3E9, 6H1 and 10B12; each mAb in the pool was at one third of the final concentration), 125 μg/ml anti-PvRBP2b polyclonal antibody R1527, 125 μg/ml mouse isotype control (ThermoFisher MA1-10407), 125 μg/ml rabbit prebleed IgG (Abcam, ab176094) or 25 μg/ml of a camelid anti-Fy6. For the rabbit polyclonal antibodies, R1527 and the prebleed control were both protein A purified total IgG. Since the camelid anti-Fy6 antibody is a single monovalent VHH domain (15 kDa), it was added at 25 μg/ml to match molar concentration and valency of the other conventional antibodies.

The *ex vivo* invasion assays used in this study for Thai isolates has been described previously (*20*, *77*). Selection of the late developmental stages of *P. vivax* was performed using the magnetic-activated cell sorting (MACS) system (Miltenyi). Mature parasites were mixed with TfR1-positive enriched reticulocytes in in either the absence or in the presence of up to 125 μg/ml of anti-PvRBP2b mAbs 3E9, 6H1, 8G7 and 10B12, 125 μg/ml of pooled anti-PvRBP2b mAbs (3E9, 6H1 and 10B12) or 25 μg/ml of a camelid anti-Fy6 antibody. Enriched reticulocytes and mature *P. vivax* schizonts were incubated together for 24 hours, and newly infected red blood cells were determined by microscopy. The Thai clinical samples used in this study were collected from *P. vivax* infected patients and healthy donors for the cord blood attending the clinics of the Shoklo Malaria Research Unit (SMRU), Mae Sot, Thailand, under the following ethical guidelines in the approved protocols; OXTREC 45-09 and OXTREC 17-11 (University of Oxford, Centre for Clinical Vaccinology and Tropical Medicine, UK) and MUTM 2008-215 from the Ethics committee of Faculty of Tropical Medicine, Mahidol University.

For the *ex vivo* assays using Brazilian isolates, TfR1-positive reticulocytes were enriched from packed O+ peripheral blood from Caucasian donors (Valley Biomedical, USA) as described previously with the following modifications (*78*). Briefly, RBCs were first centrifuged at 4,000 *x g* for 2 hours, following which the top 20% of cells were recovered. These cells were layered on a KCl-Percoll gradient (between 1.078 – 1.084 g/ml) and the cells at the interface were recovered and washed multiple times with incomplete RPMI 1640 medium (ThermoFisher, USA). White blood cell contaminants were removed by passing cells through a 45% (v/v) KCl-Percoll gradient, following which the reticulocyte-enriched pellet fraction was recovered and washed with RPMI 1640 medium. Cells were resuspended in Iscove's Modified Dulbecco's Medium (ThermoFisher, USA) and CD71 microbeads (Miltenyi Biotec, USA) were added according to the manufacturer's instructions. Cells and microbeads were incubated with rotation overnight at 4°C. Next the cells were washed to remove excess microbeads and then loaded onto an AutoMACS instrument (Miltenyi Biotec, USA). TfR1-enriched cells were recovered, washed and the proportion of TfR1-positive cells was determined via flow cytometry using anti-TfR1-APC (Miltenyi Biotec, USA). Enrichment was generally > 80% TfR1-positive.

Frozen Brazilian *P. vivax* isolates were thawed and enriched using 1.080 g/ml KCl-Percoll gradients. Parasites were subsequently cultured in Iscove's Modified Dulbecco's Medium (ThermoFisher, USA) supplemented with 10% (v/v) heat-inactivated AB+ human serum and 0.25 mg/ml gentamycin (ThermoFisher, USA) at 37°C in parasite culture gas (94% nitrogen, 5% carbon dioxide, 1% oxygen) for 40 hours. Schizontemia was determined via slide microscopy and the cell density via hemocytometer counting. Schizontemia levels were generally between 0.5 – 1.0%. Invasion assays were set up in half-area 96-well plates (Corning, USA) with 1.0 x 10^6 *P. vivax* donor cells plus 1.0 x 10^6 acceptor cells (either TfR1-positive reticulocytes or JK1 cells) in a total of 100 µl of AIM V medium (ThermoFisher, USA) supplemented with 10% (v/v) AB+ human serum and 0.25 mg/ml gentamycin (Sigma-Aldrich, USA). Where appropriate, assays with Brazilian isolates were supplemented in the absence or presence of preservative-free antibodies of 125 µg/ml of anti-PvRBP2b mAbs 3E9, 6H1, 8G7 and 10B12, 125 µg/ml pooled anti-PvRBP2b antibodies (3E9, 6H1 and 10B12), 125 µg/ml anti-PvRBP2b polyclonal antibody R1527, 125 µg/ml mouse isotype control (ThermoFisher MA1-10407), 125 µg/ml rabbit prebleed IgG (Abcam, ab176094). Invasion was allowed to proceed for ~ 20 hours at which point cytospins were made (ThermoFisher, USA). Cells were stained either with Hemacolor II stain (Sigma-Aldrich, USA) or May-Grünwald-Giemsa (Sigma-Aldrich, USA) and parasitemia was determined by slide microscopy using a Miller reticle and whole-field counting as described (*79*). Slides were counted until a minimum of 20 newly-invaded ring-stage parasites had been observed. For each experiment data were collected from between 2 – 3 technical replicates. Study protocols for parasite sample collection in Brazil were approved by the Institutional Review Board of the Institute of Biomedical Sciences, University of São Paulo, Brazil (936/CEP, 2010 and 1169/CEPSH, 2014). Written informed consent was obtained from all patients.

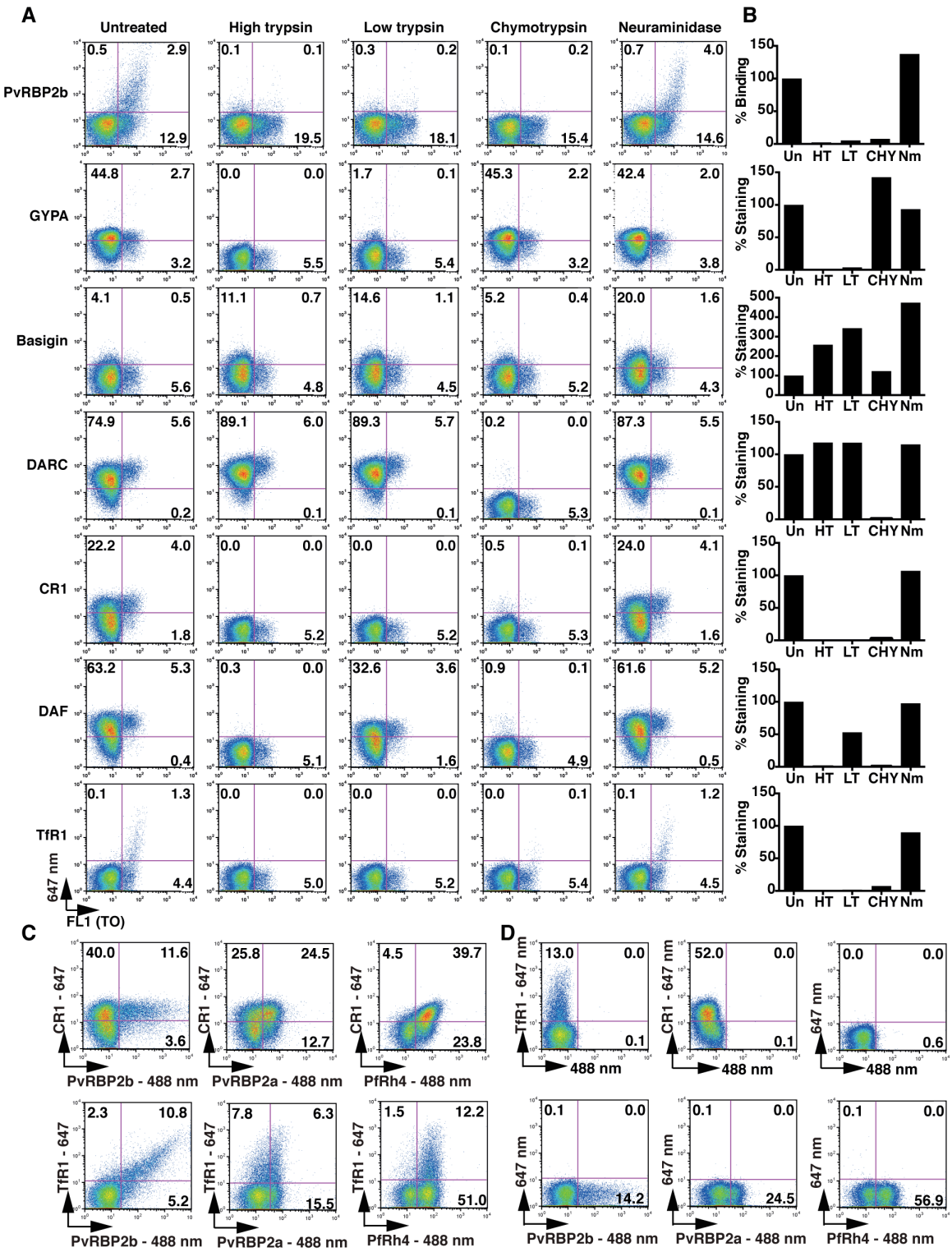

Figure S1. Flow cytometry-based analysis of PvRBP2b binding and receptor surface expression. (**A**) Dot plots of PvRBP2b binding and surface expression for glycophorin A (GYPA), basigin, DARC, CR1, Decay Accelerating Factor (DAF) and TfR1 were analyzed by flow cytometry on reticulocytes treated with low or high amounts of trypsin (LT or HT), chymotrypsin (CHY) or neuraminidase (Nm). Reticulocytes were stained

with thiazole orange (TO, x-axis). (**B**) Compiled PvRBP2b binding results and surface expression staining. (**C**) Dot plots of PvRBP2b, PvRBP2a and PfRh4 binding together with surface staining for CR1 (top panel) and TfR1 (bottom panel) were analyzed by flow cytometry on reticulocyte-enriched populations. These data show that PfRh4 binding is correlated with CR1 levels and PvRBP2b binding is correlated with TfR1 levels. (**D**) Dot plots of surface receptor expression of TfR1, CR1 and unstained cells (top panels) and reticulocytes with bound PvRBP2b, PvRBP2a and PfRh4 binding alone (bottom panel) were analyzed by flow cytometry on reticulocytes. These data shows no bleed through between the channels.

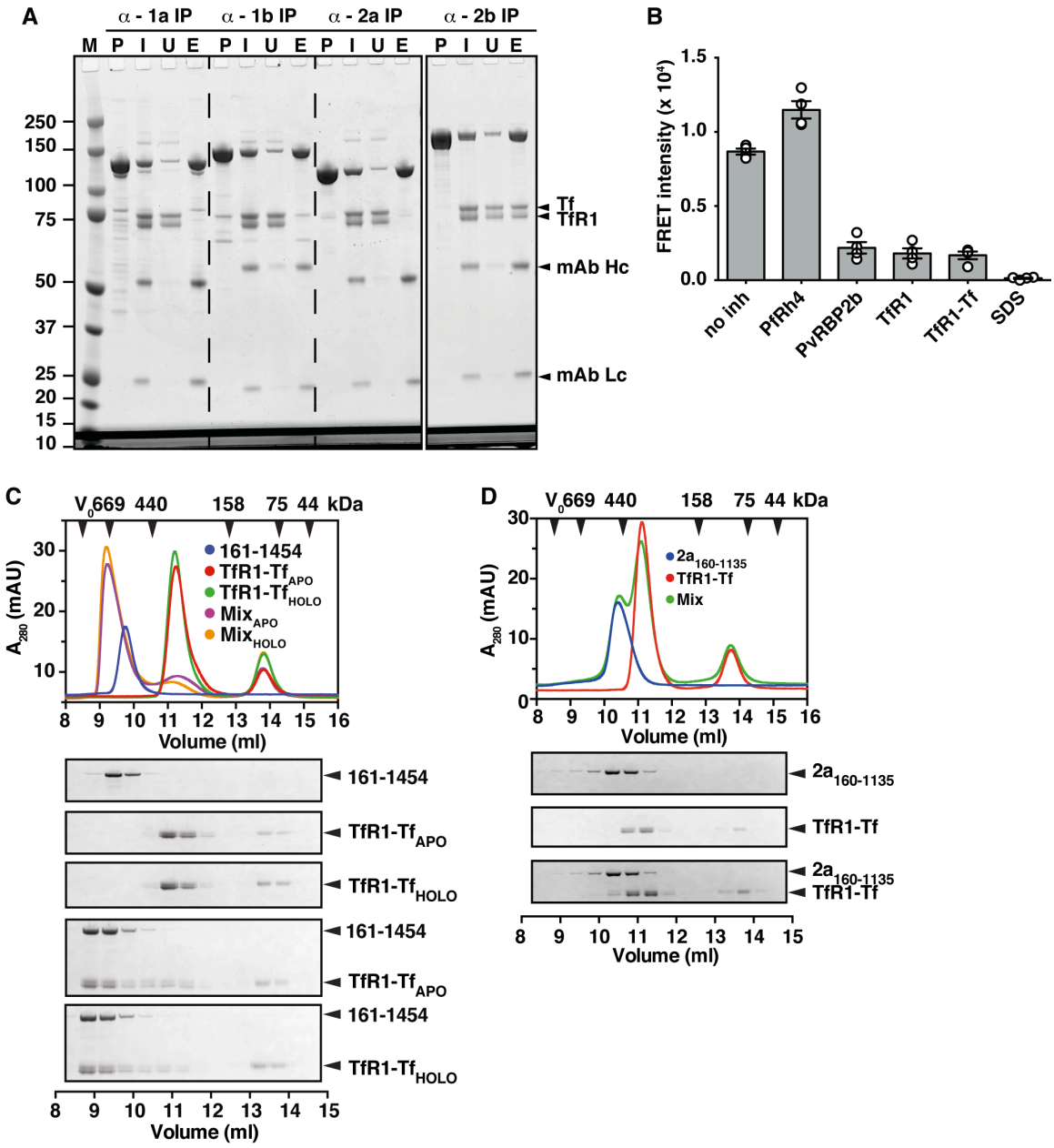

Figure S2. Specificity of the interaction between PvRBP2b and TfR1-Tf. (**A**) PvRBP1a (117 kDa), PvRBP1b (133 kDa), PvRBP2a (114 kDa) and PvRBP2b (153 kDa) were immunoprecipitated with their respective mAbs in the presence of the binary complex TfR1-Tf. Molecular weight marker (M) labeled in kDa. Eluates were run under reducing conditions on a SDS-PAGE gel and stained with SimplyBlue SafeStain. Multiple bands in the lanes with PvRBP alone suggest protein degradation or contaminating proteins from the purification of these PvRBPs that may bind non-specifically. P, PvRBP alone. I, input. U, unbound. E, eluate. (**B**) Measured FRET fluorescence intensity of the interaction between PvRBP2b-Dylight488 and TfR1-Dylight594 incubated at 1:1 molar concentration (no inh) either in the presence of unlabeled proteins (PfRh4, PvRBP2b, TfR1 and binary complex TfR1-Tf) or SDS as a denaturant. The fluorescence intensity (FI) of DyLight-488 (donor) was measured with a

485/14-nm excitation filter and a 535/25-nm emission filter and DyLight-594 was measured with a 590/20-nm excitation filter and 615/9-nm emission filter. (**C**) The interaction between PvRBP2b and TfR1-Tf binary complex is similar in the presence of iron-depleted (Tf_{APO}) and iron-loaded (Tf_{HOLO}) form of human transferrin. The exclusion volume (V_0) of the columns and the elution volumes of selected marker proteins are indicated with black arrowheads. Lower part: Coomassie-Blue stained SDS-PAGE gels of the fractions obtained from SEC. $PvRBP2b_{161-1454}$ was used in panels A, B and C. (**D**) PvRBP2a does not interact with the TfR1-Tf binary complex as analyzed by SEC.

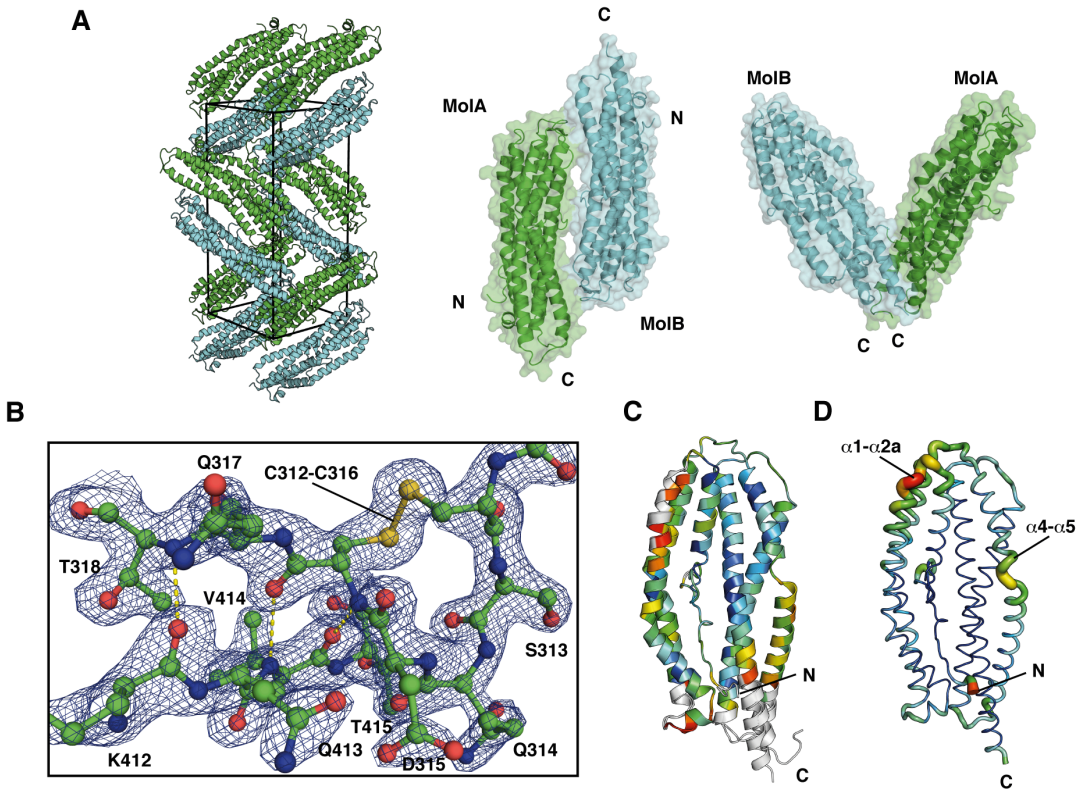

Figure S3. Detailed analyses of PvRBP2b structure. (**A**) Analysis of the packing of the molecules in the crystal. Left panel: General view of the crystal. Black lines represent the edges of the unit cell. Middle panel: Two molecules, MolA and MolB, present in the asymmetric unit can be seen in head-to-tail orientation. Both molecules consist of 301 residues spanning 169 to 470 amino acids of PvRBP2b and additionally include a di-peptide Gly-Ser fragment which was introduced as a cloning artifact. The buried interface area between two molecules present in the ASU is around 719 Å^2 as calculated using PISA server. Right panel: the most important crystal contact between molecules A and B from the neighboring asymmetric units buries around 915 Å^2 of the interface area. Molecules A and B are colored in green and cyan, respectively and shown as ribbon and surface representation. (**B**) Representative electron density around the disulphide bond formed between Cys312 and Cys316. The short beta-sheet formed between strands β3 and β4 is also visible. The $2F_{obs}$-F_{calc} map is contoured at 2σ and shown as blue mesh. Protein is shown in ball and stick representation with carbon shown in green, nitrogen in blue, oxygen in red and sulfur in yellow. The hydrogen bond network between strands β3 and β4 is shown as yellow dashed line. (**C**) Superimposition of the two molecules from the asymmetric unit. Molecules are shown as ribbons colored with the colors corresponding to the RMSD between two molecules in the range from 0.01 to 0.46 Å. Dark blue shows good alignment, higher deviations are in orange/yellow/red. Residues not used for alignment are colored white. (**D**) Analysis of B-factors. The most flexible regions include a loop interconnecting helices α1 with α2a and helices α4 with α5. Molecule is shown as cartoon putty representation. The width of the structure as well as the colors changing from blue to red are proportional to the average residue temperature factor changing in the range from 18.45 to 98.65 Å^2. The protein regions with high temperature factors are shown as wide orange/red tubes.

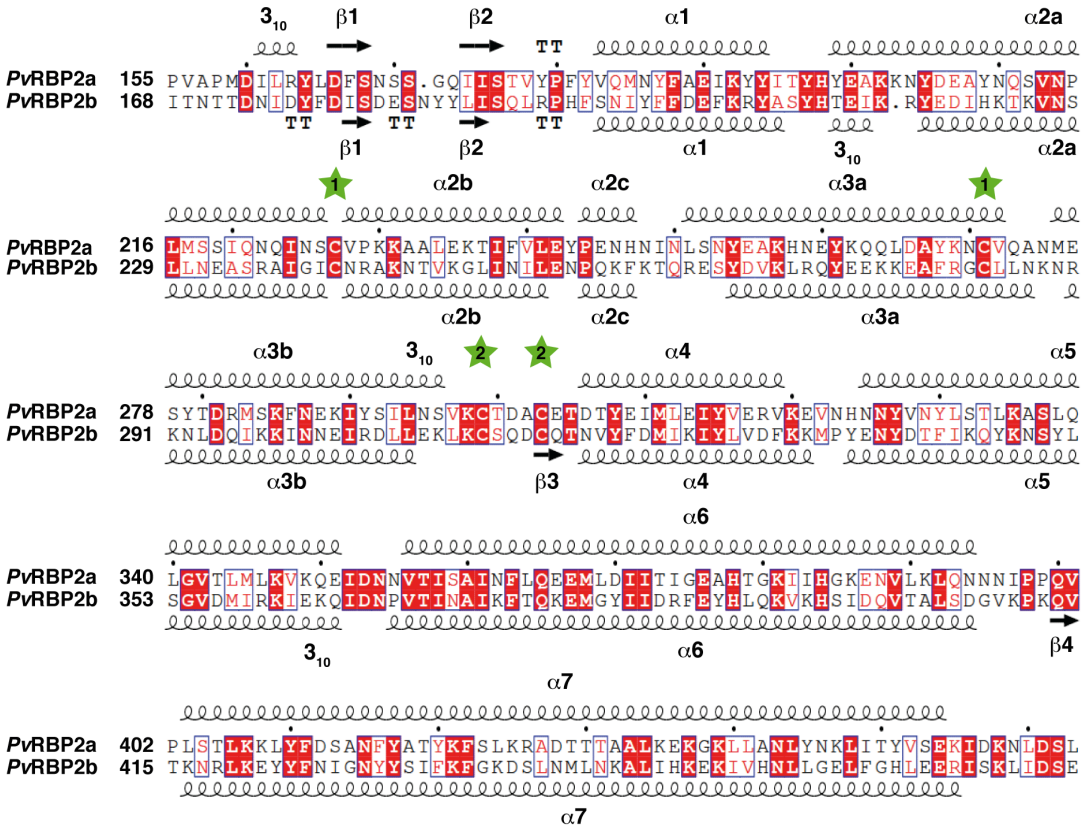

Figure S4. Sequence alignment of the crystallized fragments of PvRBP2a and PvRBP2b. The sequence alignment was generated using Clustal Omega and manually refined. The figure was prepared using ESPript3 (http://espript.ibcp.fr/ESPript/ESPript). The secondary structures of PvRBP2a and PvRBP2b are shown above and below the sequences, respectively. Identical residues are highlighted in red boxes whereas similar residues are colored red in white boxes. The positions of conserved cysteine residues are marked with green stars and labeled with corresponding numbers.

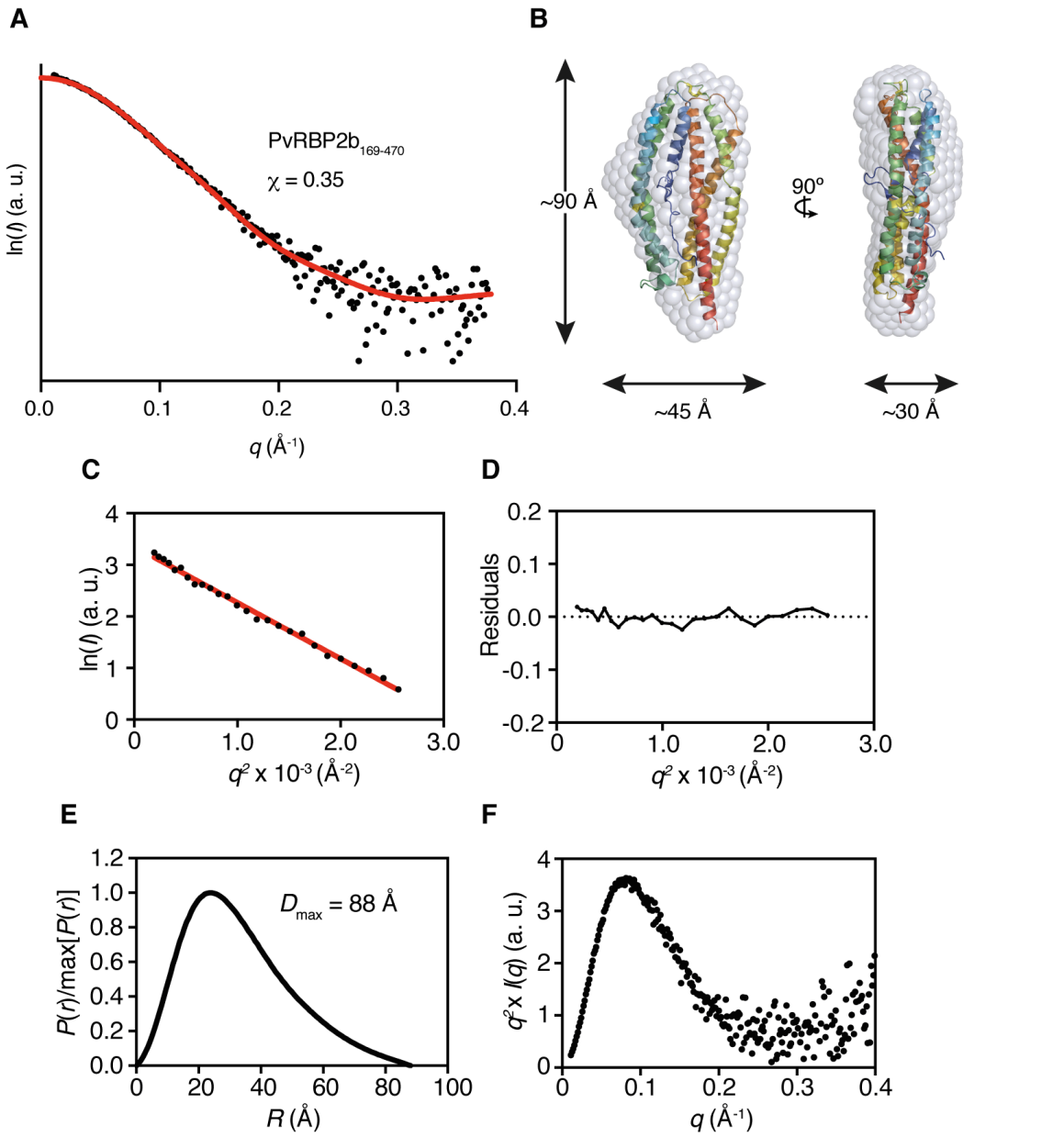

Figure S5. Small angle X-ray scattering analysis of PvRBP2b$_{169-470}$. (**A**) Scattering intensity profile for PvRBP2b$_{169-470}$. The background-subtracted SAXS data are shown as black circles representing natural logarithm of mean intensity ln$I(q)$ as a function of momentum transfer q in Å^{-1} (a.u. - arbitrary unit). The theoretical scattering profile (red line) calculated from the crystal structure was fitted to the experimental scattering data of PvRBP2b$_{169-470}$ using CRYSOL with χ value of 0.35. (**B**) Two orthogonal views of *ab initio* bead models of PvRBP2b$_{169-470}$ represented as grey spheres, superimposed with the crystal structure of the same construct. (**C**) Guinier plot for $qR_g \leq 1.3$. The radius of gyration and initial scattering intensity $I(0)$ were approximated using the Guinier equation with PRIMUS. The values are presented in Table S2. (**D**) Residuals for the Guinier plot. (**E**) Pair-wise inter-atomic distance distribution function, $P(r)$. The R_g and maximum particle dimension D_{max} calculated from the $P(r)$ analysis are as indicated in Table S2. (**F**) Kratky plot analysis of the SAXS data.

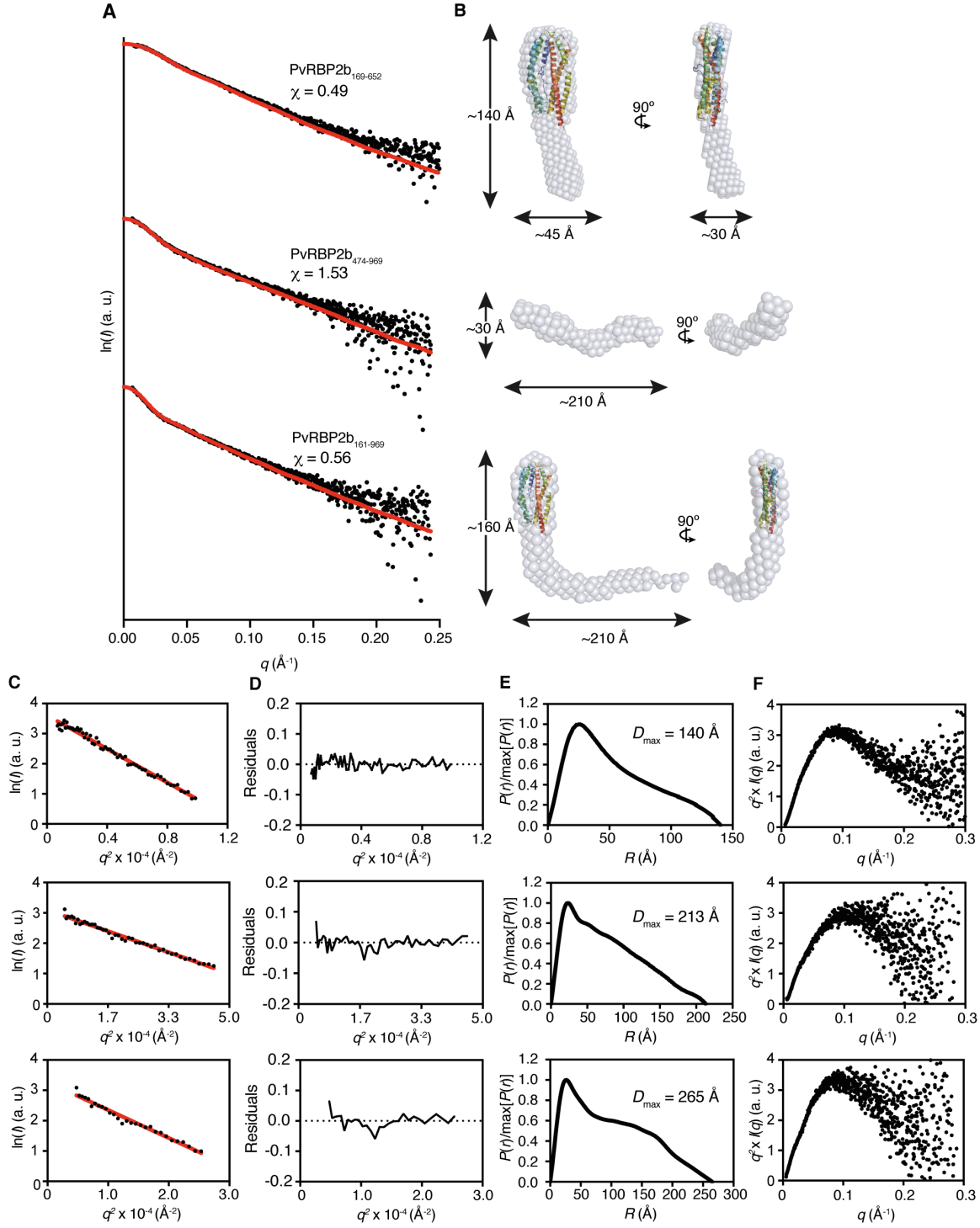

Figure S6. Small angle X-ray scattering analysis of different constructs of PvRBP2b. (**A**) Arbitrarily offset scattering intensity profiles from the apex of in-line size-exclusion column elution peaks for PvRBP2b$_{169-652}$ (top), PvRBP2b$_{474-969}$ (middle) and PvRBP2b$_{161-969}$ (bottom). The SAXS data are shown as black circles. Solid red line represents a calculated scattering pattern of an average *ab initio* model. The χ value

indicating the fit of the average model to the experimental data was calculated using CRYSOL. (**B**) Two orthogonal views of *ab initio* bead models of PvRBP2b represented as grey spheres, superimposed with crystal structure of *P. vivax* PvRBP2b$_{169-470}$: PvRBP2b$_{169-652}$ (top), PvRBP2b$_{474-969}$ (middle) and PvRBP2b$_{161-969}$ (bottom). (**C**) Guinier plots for $qR_g \leq 1.3$. (**D**) Residuals for the Guinier plot. (**E**) Pair-wise inter-atomic distance distribution function, $P(r)$. (**F**) Kratky plot analysis of the SAXS data.

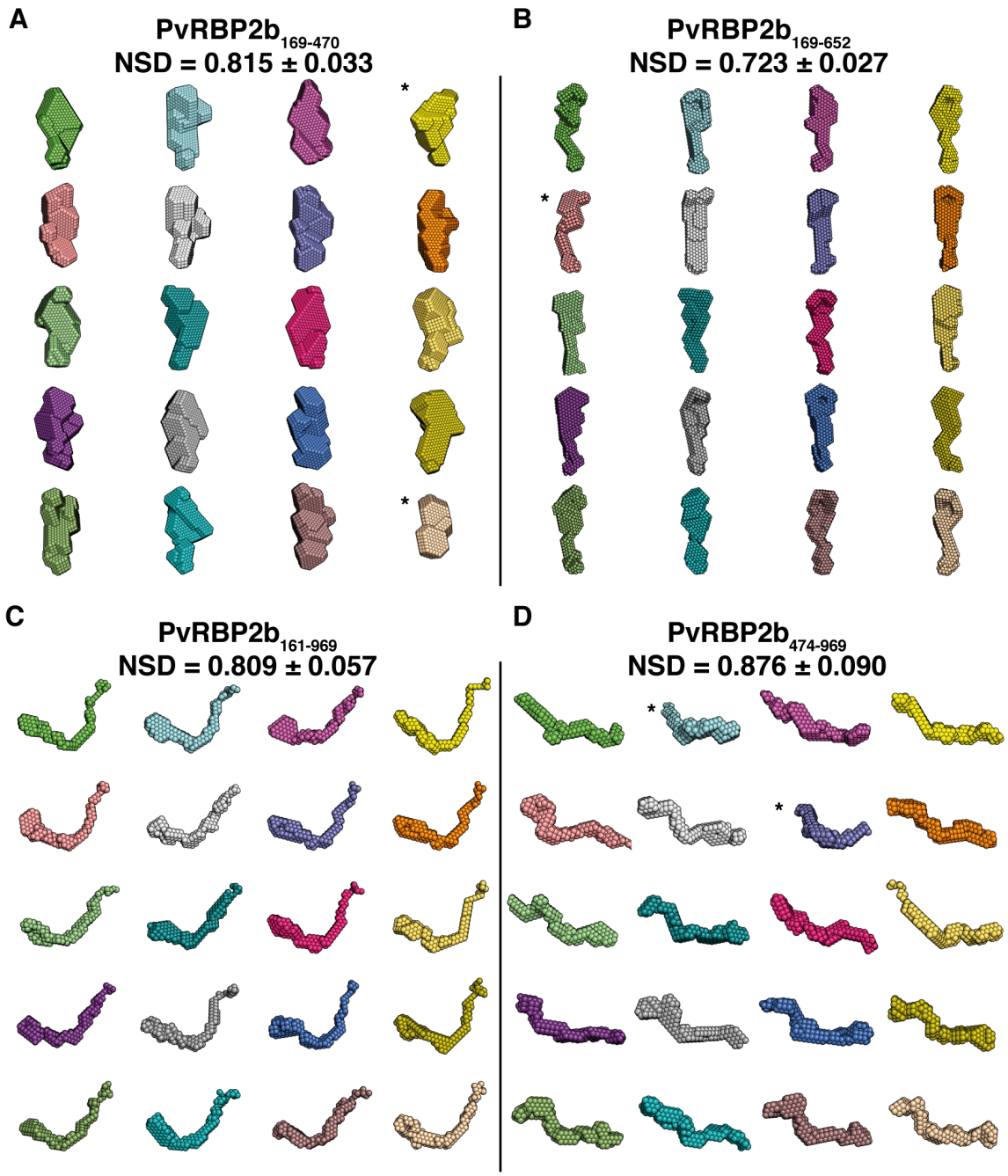

Figure S7. Twenty *ab initio* models generated using program DAMMIF based on SAXS data collected for each PvRBP2b fragment. (**A**) PvRBP2b$_{169\text{-}470}$. (**B**) PvRBP2b$_{169\text{-}652}$. (**C**) PvRBP2b$_{161\text{-}969}$. (**D**) PvRBP2b$_{474\text{-}969}$. * indicates the models that were not included in averaging due to their normalized spatial discrepancy parameter NSD being higher than the mean value plus two times standard deviation.

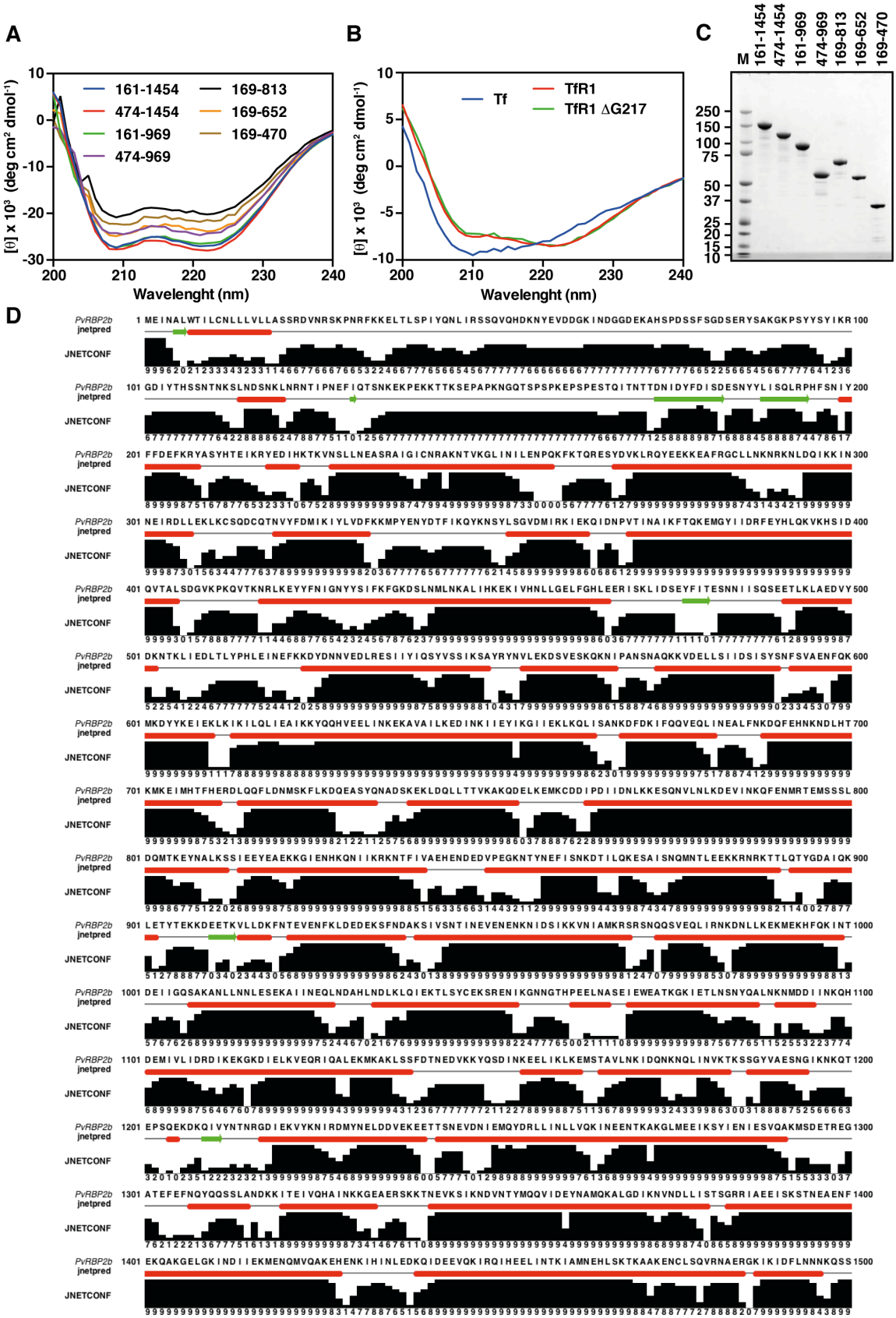
A
B
C
D
161-1454
474-1454
161-969
474-969
169-813
169-652
169-470
[θ] x 10³ (deg cm² dmol⁻¹)
Wavelenght (nm)
Tf
TfR1
TfR1 ΔG217
M
250
150
100
75
50
37
25
20
15
10
PvRBP2b
jnetpred
JNETCONF

Figure S8. Circular dichroism spectra of recombinant PvRBP2b variants, Tf and TfR1. Circular dichroism spectra of recombinant PvRBP2b variants (**A**) and Tf, TfR1 and TfR1 ΔG217 mutant (**B**). The signal is presented as mean residue molar ellipticity (θ). (**C**) SDS-PAGE gel of purified PvRBP2b recombinant proteins. Two micrograms of each protein were loaded onto a 4-12% NuPAGE gradient gel under reducing conditions and stained with Coomassie Brilliant Blue. Molecular mass marker (M) indicated in kDa. (**D**) Secondary structures prediction for PvRBP2b (residues 1-1,500) obtained using JNet. JNetPRED represents the consensus prediction with helices marked as red tubes and sheets as green arrows. JNetCONF shows the confidence estimate for the prediction. High values mean high confidence.

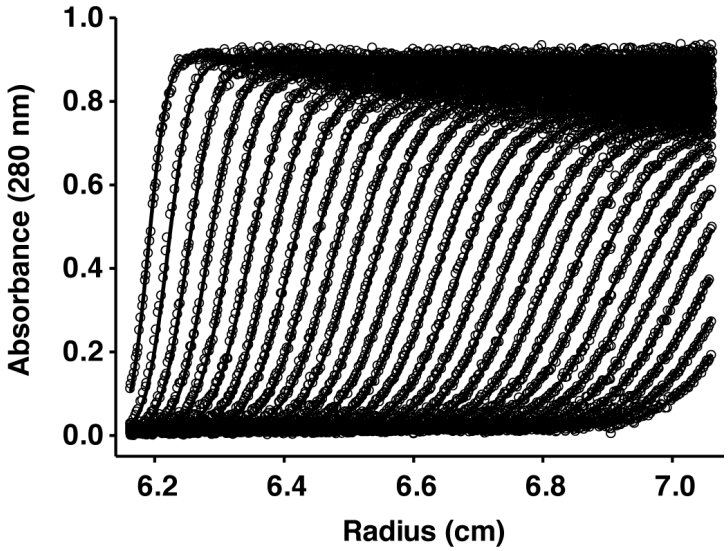

Figure S9. Sedimentation velocity analysis of transferrin receptor-transferrin complex binding to PvRBP2b$_{161\text{-}969}$. Radial scans from the analytical ultracentrifuge are shown as circles, and the best fit to a continuous sedimentation coefficient distribution shown as solid lines.

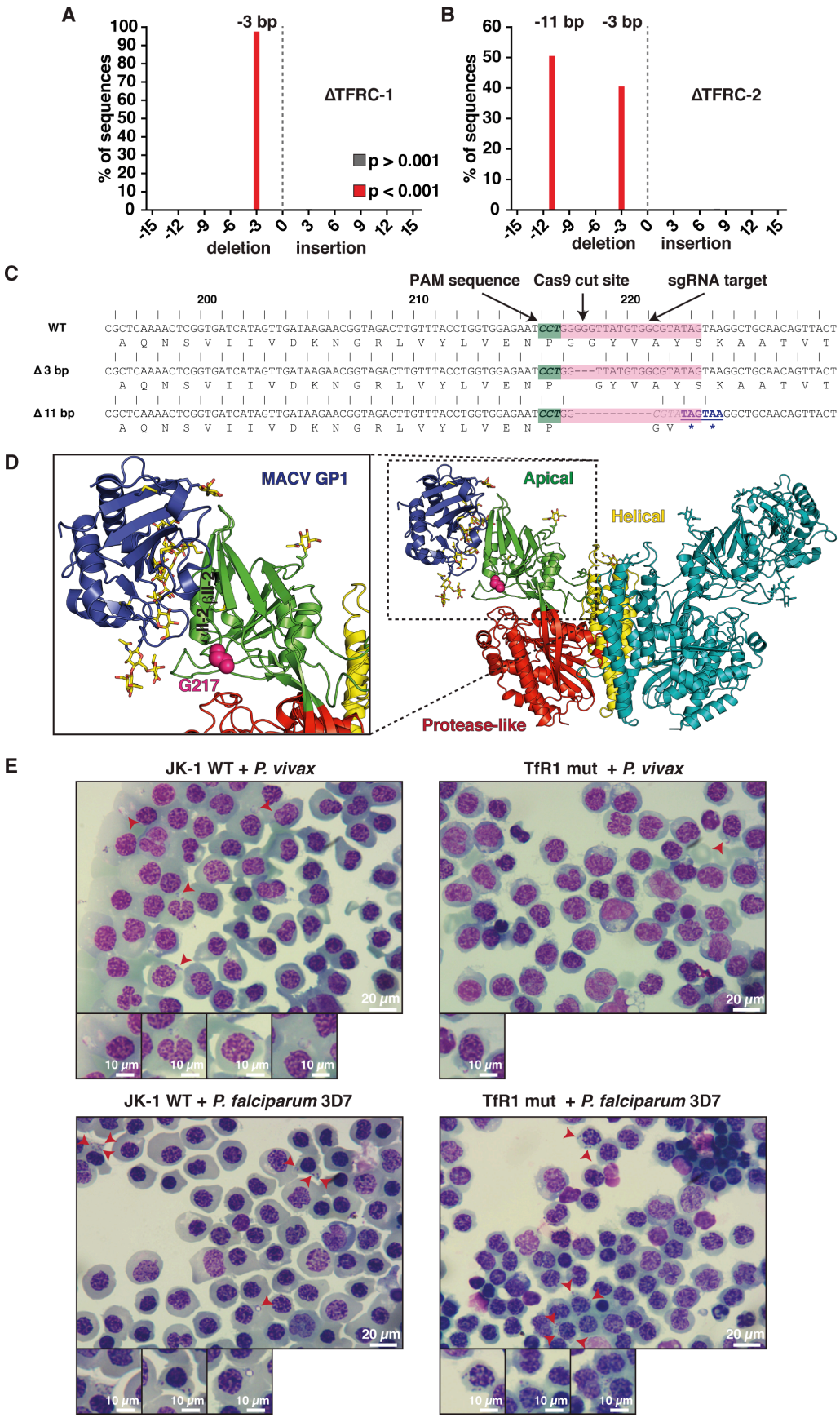
A
-3 bp
ΔTFRC-1
% of sequences
p > 0.001
p < 0.001
deletion
insertion
B
-11 bp
-3 bp
ΔTFRC-2
C
PAM sequence
Cas9 cut site
sgRNA target
WT
Δ 3 bp
Δ 11 bp
D
MACV GP1
JK-1
G217
Apical
Helical
Protease-like
E
JK-1 WT + P. vivax
TfR1 mut + P. vivax
JK-1 WT + P. falciparum 3D7
TfR1 mut + P. falciparum 3D7
20 μm
10 μm

Figure S10. Identification of TFRC mutations introduced by CRISPR/Cas9. TIDE analysis of the two TFRC clones shows that ΔTFRC-1 is homozygous for a -3 bp deletion (**A**) while ΔTFRC-2 is a heterozygote, containing both a -3 bp and a -11 bp deletion (**B**). (**C**) The sgRNA target site (salmon) is shown along with the PAM sequences and the Cas9-cut site. The exact size and location of the -3 bp and -11 bp deletions are shown and have been identified from Sanger sequencing data. The -3 bp deletion results in the in-frame loss of Gly217, while the -11 bp deletion results in a premature stop codon. (**D**) The position of residue Gly217 (magenta spheres) mapped on the crystal structure of TfR1 ectodomain bound to MACV GP1 (PDB ID: 3KAS). The Gly217 mutation is localized in the loop lying in the close vicinity of helix αII-2 and sheet βII-2 that are the main interaction sites with MACV GP1. The particular domains in one monomer of TfR1 are colored with protease-like domain shown in red, helical domain in yellow and the apical domain in green. The other molecule of TfR1 is shown in cyan. MACV GP1 is shown in blue. N-linked glycan moieties decorating the surface of both proteins are shown as sticks. (**E**) Light microscopy images of parasite invasion. Invasion of *P. vivax* into JK-1 WT (top left) and TfR1 mut cells (top right) and invasion of *P. falciparum* 3D7 into JK-1 WT (bottom left) and TfR1 mut cells (bottom right). Parasitized cells are indicated by red arrows. Insets show close-up views of infected cells.

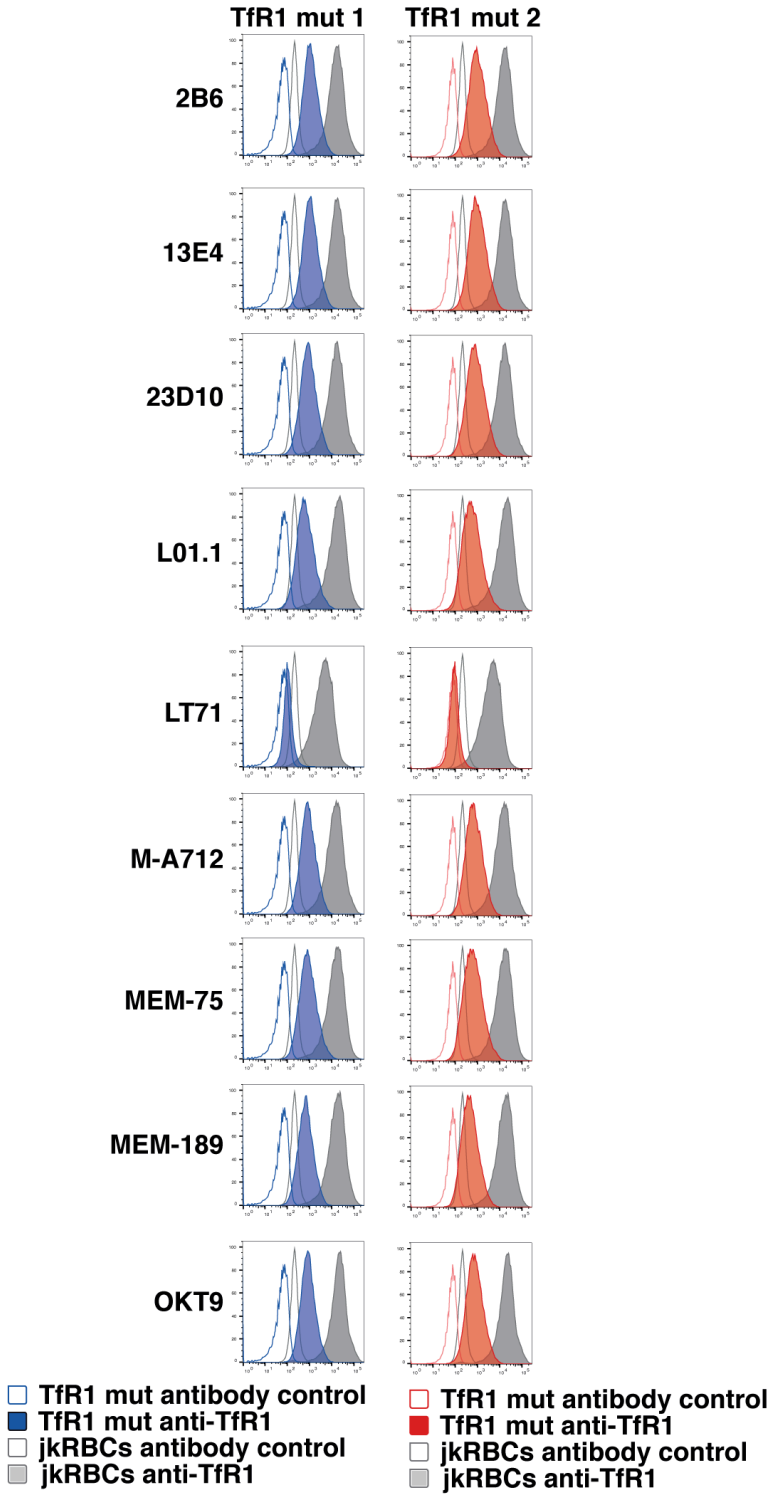

Figure S11. Expression of TfR1 on the surface of jkRBC and TfR1 mutant cells as measured by flow cytometry using nine anti-TfR1 monoclonal antibodies as indicated. The antibody control reflects the staining of the secondary antibody alone.

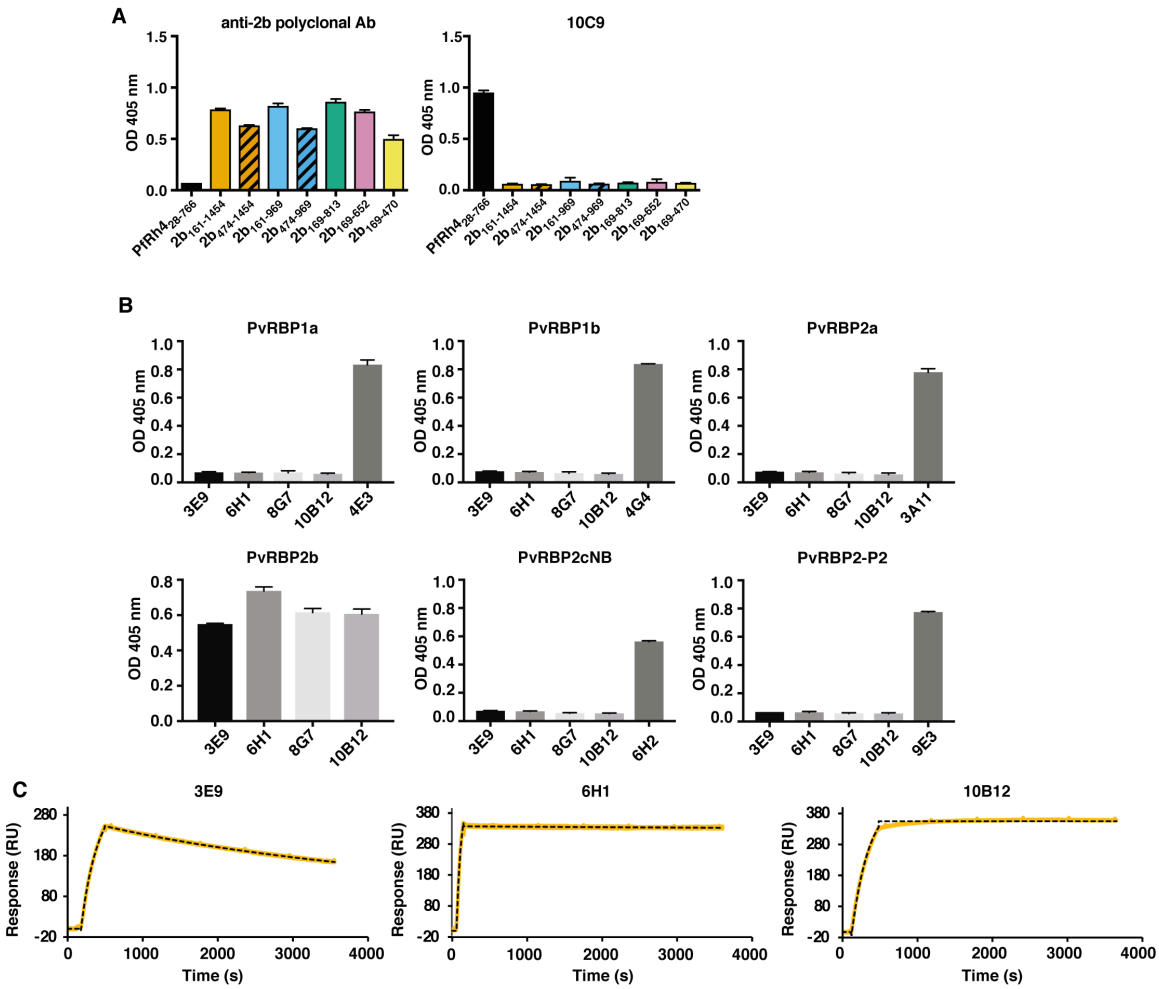

Figure S12. Detection of recombinant PvRBP2b fragments by ELISA. (**A**) ELISA plates were coated with equimolar concentrations of each recombinant fragment and detection with anti-PvRBP2b rabbit polyclonal antibody (left) and anti-PfRh4 mAb 10C9 (right) are shown. Representative plot of n=3 is shown and error bars represent range of duplicate measurement per experiment. (**B**) ELISA plates were coated with equimolar concentrations of each recombinant fragment (top label) and detection with primary monoclonal antibodies against PvRBP1a (4E3), PvRBP1b (4G4), PvRBP2a (3A11), PvRBP2b (3E9, 6H1, 8G7 and 10B12), PvRBP2cNB (6H2) and PvRBP2-P2 (9E3) are shown. Representative plot of n=2 is shown and error bars represent range of duplicate measurement per experiment. (**C**) Interaction between anti-PvRBP2b monoclonal antibodies and PvRBP2b measured by SPR. PvRBP2b$_{161\text{-}1454}$ was immobilized via standard amine coupling onto carboxymethyldextran sensorchips and 3E9, 6H1 and 10B12 mAbs were flown over the surfaces at the concentrations 40, 52 and 40 nM, respectively. The binding curves were fit to a bivalent (2:1) interaction model. Sensorgrams of the interaction are displayed in yellow and the fitted curves are displayed as black dashes; RU - resonance units.

Table S1. Crystallographic data collection and refinement statistics.

	PvRBP2b$_{169\text{-}470}$
Data collection statistics	
Space group	*P* 1 2_1 1
Unit-cell dimensions	
a, b, c (Å)	59.50, 124.20, 65.31
α, β, γ (°)	90.00, 97.75, 90.00
Wavelength (Å)	0.95370
Resolution (Å)	34.87 - 1.71 (1.74 - 1.71)
Number of unique reflections	100,494 (4,872)
R_{merge}[a]	0.11 (1.71)
R_{pim}[b]	0.04 (0.66)
$\langle I/\sigma I \rangle$	10.0 (1.2)
Completeness (%)	99.4 (98.8)
Multiplicity	7.4 (7.5)
$CC_{1/2}$[c]	0.996 (0.551)
Wilson B-factor (Å^2)	25.1
Refinement statistics	
Resolution (Å)	34.17 - 1.71 (1.80 - 1.71)
Unique reflections	100,440
R_{work}[d]	0.168 (0.273)
R_{free}[d]	0.188 (0.305)
Number of atoms	5947
Protein	5100
Ligand	23
Solvent	824
Average B-factors (Å^2)	35.5
Protein	33.8
Ligands	54.1
Solvent	45.3
R.m.s. deviations	
Bond lengths (Å)	0.014
Bond angles (°)	1.32
Ramachandran plot (%)	
Most favored	98.2
Allowed	1.8
Outlier	0

Statistics for the highest-resolution shell are shown in parentheses.
Data were collected on a single crystal.
[a] $R_{merge} = \Sigma_{hkl}\Sigma_i \left| I_i(hkl) - \langle I(hkl) \rangle \right| / \Sigma_{hkl} \Sigma_i I_i(hkl)$ (*80*).
[b] $R_{pim} = \Sigma_{hkl} \{1/[N(hkl) - 1]\}^{1/2} \times \Sigma_j \left| I_i(hkl) - \langle I(hkl) \rangle \right| / \Sigma_{hkl} \Sigma_j I_i(hkl)$ (*81*).
[c] $CC_{1/2}$ = Pearson correlation coefficient between independently merged halves of the data set (*82*).
[d] $R_{work} = \Sigma_{hkl} \left| F_o(hkl) - F_c(hkl) \right| / \Sigma_{hkl} F_o(hkl)$. R_{free} was calculated for a test set of reflections omitted from the refinement.

Table S2. SAXS data collection and analysis statistics.

Data-collection parameters	
Instrument	Australian Synchrotron SAXS/WAXS beamline
Beam geometry	120 μm point source
Wavelength (Å)	1.033
Exposure time (s)	2
Protein concentration	between 3.0 and 8.0 mg/ml via in-line gel filtration chromatography
Temperature (°C)	16
Software employed	
Primary data reduction	ScatterBrain (Australian Synchrotron)
Data processing	PRIMUS, GNOM
Ab initio modelling	DAMMIF, DAMSEL, DAMSUP, DAMAVER, DAMFILT
Rigid-body modelling	COLORES
3D graphics representations	MacPyMOL

Structural parameters	$PvRBP2b_{169-470}$	$PvRBP2b_{169-652}$	$PvRBP2b_{474-969}$	$PvRBP2b_{161-969}$
$I(0)$ (cm^{-1}) from $P(r)$	0.01316 ± 0.00012	0.01411 ± 0.00012	0.01143 ± 0.00006	0.01231 ± 0.00007
R_g (Å) from $P(r)$	25.96 ± 0.32	43.79 ± 0.42	63.99 ± 0.40	82.03 ± 0.49
D_{max} (Å)	88 ± 2	140 ± 3	213 ± 5	265 ± 7
$I(0)$ (cm^{-1}) from Guinier	0.013 ± 0.001	0.014 ± 0.001	0.011 ± 0.001	0.012 ± 0.001
R_g (Å) from Guinier	25.40 ± 0.52	41.3 ± 0.80	60.60 ± 0.61	81.40 ± 1.00

Table S3. List of the oligonucleotides used in this study to create different variants of PvRBP2b protein.

Oligonucleotide	Construct	Vector	Sequence
JG125	$PvRBP2b_{169-470}$	pPROEX HTb	AAC CTG TAT TTT CAG GGC GCC ATG GGA TCC ACC AAT ACC ACC GAT AAC ATC GAT
JG126			GCC AAG CTT GGT ACC GCA TGC CTC GAG TCA GCT AAT ACG TTC TTC CAG ATG ACC
JG125	$PvRBP2b_{169-652}$	pPROEX HTb	AAC CTG TAT TTT CAG GGC GCC ATG GGA TCC ACC AAT ACC ACC GAT AAC ATC GAT
JG213			GCC AAG CTT GGT ACC GCA TGC CTC GAG TCA ATA TTC GAT AAT TTT GTT AAT ATC TTC TTT
JG125	$PvRBP2b_{169-813}$	pPROEX HTb	AAC CTG TAT TTT CAG GGC GCC ATG GGA TCC ACC AAT ACC ACC GAT AAC ATC GAT
JG215			GCC AAG CTT GGT ACC GCA TGC CTC GAG TCA GCT GGA CTT CAG GGC ATT ATA TTC TTT GGT
JG51	$PvRBP2b_{161-969}$	pET-32a(+)	TAA TAC GAC TCA CTA TAG GGG
JG159			TTG TTC AAC GCT CTG CTG ATT GCT TCA GCT ACG TTT CAT GGC AAT ATT CAC TTT
JG160	$PvRBP2b_{474-969}$	pET-32a(+)	CTG TAT TTT CAG GGC GCC ATG GGA TCC GAT AGC GAG TAT TTT ATC ACC GAA AGC
JG159			TTG TTC AAC GCT CTG CTG ATT GCT TCA GCT ACG TTT CAT GGC AAT ATT CAC TTT
JG160	$PvRBP2b_{474-1454}$	pET-32a(+)	CTG TAT TTT CAG GGC GCC ATG GGA TCC GAT AGC GAG TAT TTT ATC ACC GAA AGC
JG161			GCT TTC GGT GAT AAA ATA CTC GCT ATC GGA TCC CAT GGC GCC CTG AAA ATA CAG
JG71	$PvRBP2b_{161-1454}$	PET-32a(+)	GGT TCT GAA AAC CTG TAT TTT CAG GGC GCC AAC ATC GAT TAC TTC GAT ATT TCC
JG73			GCT TTG TTA GCA GCC GGA TCT CAG TCA TGC CTG TTT TTC AAA GTT TTC GG

Table S4. Molecular weights and absorption coefficients for the proteins used in this study.

Protein name	MW (kDa)	A_{280} 0.1%	ε_{280} ($M^{-1}cm^{-1}$)	Source
$PvRBP2b_{169-470}$	36.46	0.868	31,540	ExPASy
$PvRBP2b_{169-652}$	57.88	0.880	50,910	ExPASy
$PvRBP2b_{169-813}$	76.89	0.701	53,890	ExPASy
$PvRBP2b_{161-969}$	96.68	0.619	59,850	ExPASy
$PvRBP2b_{161-1454}$	152.9	0.545	83,355	ExPASy
$PvRBP2b_{474-969}$	58.73	0.482	28,310	ExPASy
$PvRBP2b_{474-1454}$	114.9	0.451	51,815	ExPASy
Tf	79.60[a]	1.305	103,900	(*45*)
$(TfR1)_2$	156.6[b]	1.198	187,580	(*43*)
$(TfR1\text{-}Tf)_2$	315.8[c]	1.252	395,380	(*43*, *45*)

[a]Theoretical MW = 77.06 kDa. The value in the table was obtained using mass spectrometry and reflects glycosylation of the protein.
[b]Theoretical $MW_{monomer}$ = 73.82 kDa. The value in the table was obtained using mass spectrometry and reflects glycosylation of the protein. The protein forms a homodimer.
[c]The proteins form a 2:2 complex.

Table S5. Analytical size exclusion chromatography.
(A) Molecular weights of high- and mid-mass molecular mass markers used for the calibration of the analytical size exclusion column. (B) Experimental molecular weights for the particular proteins.

A

Protein name	MW[a] (Da)	$\log_{10}$ MW	V_e[b] (ml)	K_{av}[c]
aprotinin	6,500	3.8129	19.51	0.7334
ribonuclease	13,700	4.1367	17.82	0.6221
carbonic anhydrase	29,000	4.4624	16.41	0.5293
ovoalbumin	44,000	4.6435	15.06	0.4404
conalbumin	75,000	4.8751	14.24	0.3864
aldolase	158,000	5.1987	12.81	0.2923
ferritin	440,000	5.6435	10.55	0.1435
thyroglobulin	669,000	5.8254	9.24	0.0573

B

Protein name	V_e[a] (ml)	K_{av}[b]	Calculated MW (kDa)	Theoretical MW (kDa)
$PvRBP2b_{169-470}$	16.21	0.5161	29.67	36.46
$PvRBP2b_{161-969}$	11.36	0.1968	280.0	96.68
$PvRBP2b_{474-969}$	12.27	0.2567	183.8	58.73
$PvRBP2b_{161-1454}$	9.69	0.0869	606.6	152.9
$PvRBP2b_{474-1454}$	10.04	0.1099	515.9	114.9
Tf	13.76	0.3548	92.21	79.60
$(TfR1)_2$	13.49	0.3371	104.5	156.6
$(TfR1\text{-}Tf)_2$	11.21	0.1870	300.2	315.8
$(PvRBP2b_{161-969}\text{-}TfR1\text{-}Tf)_2$	10.10	0.1139	501.8	509.2
$(PvRBP2b_{161-1454}\text{-}TfR1\text{-}Tf)_2$	9.11	0.0487	793.4	621.6

[a]MW – molecular weight
[b]V_e – elution volume
[c]$K_{av} = (V_e - V_0)/(V_c - V_0)$, partition coefficient, where V_0 = 8.37 ml, column void volume obtained using a sample of blue dextran 2000 and V_c = 23.56 ml, geometric column volume. $K_{av} = -0.3275 \times \log_{10}MW + 1.9808$, $R^2 = 0.9971$.

Table S6. SPR measurements of mAbs-PvRBP2b interactions.

mAb	k_{a1} ($M^{-1}s^{-1}$)	k_{d1} (s^{-1})	K_{D1} (M)	k_{a2} ([signal]$^{-1}s^{-1}$)	k_{d2} (s^{-1})	K_{D2} (M)	χ^2 ([signal]^2)	R_{max} (calculated)
3E9	7.1×10^{4}	3.7×10^{-4}	5.2×10^{-9}	5.8×10^{-2}	7.2×10^{0}	1.2×10^{2}	1.6	541
6H1	1.6×10^{5}	4.9×10^{-4}	3.0×10^{-9}	8.1×10^{-3}	1.3×10^{2}	1.6×10^{0}	5.3	848
10B12	5.5×10^{4}	4.9×10^{-7}	8.8×10^{-12}	2.3×10^{-1}	5.4×10^{-3}	2.4×10^{-2}	36	898

The binding curves obtained from the experiment were fit to a bivalent (2:1) interaction model to estimate affinity constants for the bivalent interaction.

Additional Database

Dataset S1. Quantitative surface proteomics analysis comparing WT jkRBCs and TfR1 mut1 and TfR1 mut2 jkRBC lines. For each protein, the following data fields are shown: UniProt ID; Gene Symbol; Description, Gene Ontology Cellular Compartment-term classification: M – membrane, PM – plasma membrane, IPM – integral to plasma membrane, CS – cell surface, XC – extracellular, Nuc – nuclear, ShG – short GO) **(*52*, *83*)**; number of identified peptides, fold change (FC) of average jkRBC signal:noise (S:N) compared to the average TfR1 Mut-1/2 (S:N); normalized S:N for each protein. The "No_Filter" worksheet includes all identified proteins and the "PM_CS_XC_ShG_2_peptides" worksheet shows the subset of plasma membrane proteins.